Revised Version DESY 96-039

DESY 96-039
March 1996
ISSN 0418-9833

A Measurement and QCD Analysis of the Proton Structure Function $F_2(x, Q^2)$ at HERA

H1 Collaboration

Abstract:

A new measurement of the proton structure function $F_2(x, Q^2)$ is reported for momentum transfers squared Q^2 between 1.5 GeV^2 and 5000 GeV^2 and for Bjorken x between $3 \cdot 10^{-5}$ and 0.32 using data collected by the HERA experiment H1 in 1994. The data represent an increase in statistics by a factor of ten with respect to the analysis of the 1993 data. Substantial extension of the kinematic range towards low Q^2 and x has been achieved using dedicated data samples and events with initial state photon radiation. The structure function is found to increase significantly with decreasing x, even in the lowest accessible Q^2 region. The data are well described by a Next to Leading Order QCD fit and the gluon density is extracted.

S. Aid[14], V. Andreev[26], B. Andrieu[29], R.-D. Appuhn[12], M. Arpagaus[37], A. Babaev[25], J. Bähr[36], J. Bán[18], Y. Ban[28], P. Baranov[26], E. Barrelet[30], R. Barschke[12], W. Bartel[12], M. Barth[5], U. Bassler[30], H.P. Beck[38], H.-J. Behrend[12], A. Belousov[26], Ch. Berger[1], G. Bernardi[30], R. Bernet[37], G. Bertrand-Coremans[5], M. Besançon[10], R. Beyer[12], P. Biddulph[23], P. Bispham[23], J.C. Bizot[28], V. Blobel[14], K. Borras[9], F. Botterweck[5], V. Boudry[29], A. Braemer[15], W. Braunschweig[1], V. Brisson[28], D. Bruncko[18], C. Brune[16], R. Buchholz[12], L. Büngener[14], J. Bürger[12], F.W. Büsser[14], A. Buniatian[12,39], S. Burke[19], M.J. Burton[23], G. Buschhorn[27], A.J. Campbell[12], T. Carli[27], F. Charles[12], M. Charlet[12], D. Clarke[6], A.B. Clegg[19], B. Clerbaux[5], S. Cocks[20], J.G. Contreras[9], C. Cormack[20], J.A. Coughlan[6], A. Courau[28], M.-C. Cousinou[24], G. Cozzika[10], L. Criegee[12], D.G. Cussans[6], J. Cvach[31], S. Dagoret[30], J.B. Dainton[20], W.D. Dau[17], K. Daum[35], M. David[10], C.L. Davis[19], B. Delcourt[28], A. De Roeck[12], E.A. De Wolf[5], M. Dirkmann[9], P. Dixon[19], P. Di Nezza[33], W. Dlugosz[8], C. Dollfus[38], J.D. Dowell[4], H.B. Dreis[2], A. Droutskoi[25], D. Düllmann[14], O. Dünger[14], H. Duhm[13], J. Ebert[35], T.R. Ebert[20], G. Eckerlin[12], V. Efremenko[25], S. Egli[38], R. Eichler[37], F. Eisele[15], E. Eisenhandler[21], R.J. Ellison[23], E. Elsen[12], M. Erdmann[15], W. Erdmann[37], E. Evrard[5], A.B. Fahr[14], L. Favart[28], A. Fedotov[25], D. Feeken[14], R. Felst[12], J. Feltesse[10], J. Ferencei[18], F. Ferrarotto[33], K. Flamm[12], M. Fleischer[9], M. Flieser[27], G. Flügge[2], A. Fomenko[26], B. Fominykh[25], J. Formánek[32], J.M. Foster[23], G. Franke[12], E. Fretwurst[13], E. Gabathuler[20], K. Gabathuler[34], F. Gaede[27], J. Garvey[4], J. Gayler[12], M. Gebauer[36], A. Gellrich[12], H. Genzel[1], R. Gerhards[12], A. Glazov[36], U. Goerlach[12], L. Goerlich[7], N. Gogitidze[26], M. Goldberg[30], D. Goldner[9], K. Golec-Biernat[7], B. Gonzalez-Pineiro[30], I. Gorelov[25], C. Grab[37], H. Grässler[2], R. Grässler[2], T. Greenshaw[20], R. Griffiths[21], G. Grindhammer[27], A. Gruber[27], C. Gruber[17], J. Haack[36], D. Haidt[12], L. Hajduk[7], M. Hampel[1], W.J. Haynes[6], G. Heinzelmann[14], R.C.W. Henderson[19], H. Henschel[36], I. Herynek[31], M.F. Hess[27], W. Hildesheim[12], K.H. Hiller[36], C.D. Hilton[23], J. Hladký[31], K.C. Hoeger[23], M. Höppner[9], D. Hoffmann[12], T. Holtom[20], R. Horisberger[34], V.L. Hudgson[4], M. Hütte[9], H. Hufnagel[15], M. Ibbotson[23], H. Itterbeck[1], A. Jacholkowska[28], C. Jacobsson[22], M. Jaffre[28], J. Janoth[16], T. Jansen[12], L. Jönsson[22], K. Johannsen[14], D.P. Johnson[5], L. Johnson[19], H. Jung[10], P.I.P. Kalmus[21], M. Kander[12], D. Kant[21], R. Kaschowitz[2], U. Kathage[17], J. Katzy[15], H.H. Kaufmann[36], O. Kaufmann[15], S. Kazarian[12], I.R. Kenyon[4], S. Kermiche[24], C. Keuker[1], C. Kiesling[27], M. Klein[36], C. Kleinwort[12], G. Knies[12], T. Köhler[1], J.H. Köhne[27], H. Kolanoski[3], F. Kole[8], S.D. Kolya[23], V. Korbel[12], M. Korn[9], P. Kostka[36], S.K. Kotelnikov[26], T. Krämerkämper[9], M.W. Krasny[7,30], H. Krehbiel[12], D. Krücker[2], U. Krüger[12], U. Krüner-Marquis[12], H. Küster[22], M. Kuhlen[27], T. Kurča[36], J. Kurzhöfer[9], D. Lacour[30], B. Laforge[10], R. Lander[8], M.P.J. Landon[21], W. Lange[36], U. Langenegger[37], J.-F. Laporte[10], A. Lebedev[26], F. Lehner[12], C. Leverenz[12], S. Levonian[29], Ch. Ley[2], G. Lindström[13], M. Lindstroem[22], J. Link[8], F. Linsel[12], J. Lipinski[14], B. List[12], G. Lobo[28], H. Lohmander[22], J.W. Lomas[23], G.C. Lopez[13], V. Lubimov[25], D. Lüke[9,12], N. Magnussen[35], E. Malinovski[26], S. Mani[8], R. Maraček[18], P. Marage[5], J. Marks[24], R. Marshall[23], J. Martens[35], G. Martin[14], R. Martin[20], H.-U. Martyn[1], J. Martyniak[7], T. Mavroidis[21], S.J. Maxfield[20], S.J. McMahon[20], A. Mehta[6], K. Meier[16], T. Merz[36], A. Meyer[14], A. Meyer[12], H. Meyer[35], J. Meyer[12], P.-O. Meyer[2], A. Migliori[29], S. Mikocki[7], D. Milstead[20], J. Moeck[27], F. Moreau[29], J.V. Morris[6], E. Mroczko[7], D. Müller[38], G. Müller[12], K. Müller[12], P. Murín[18], V. Nagovizin[25], R. Nahnhauer[36], B. Naroska[14], Th. Naumann[36], P.R. Newman[4], D. Newton[19], D. Neyret[30], H.K. Nguyen[30], T.C. Nicholls[4], F. Niebergall[14], C. Niebuhr[12], Ch. Niedzballa[1], H. Niggli[37], R. Nisius[1], G. Nowak[7], G.W. Noyes[6], M. Nyberg-Werther[22], M. Oakden[20], H. Oberlack[27], U. Obrock[9], J.E. Olsson[12], D. Ozerov[25], P. Palmen[2], E. Panaro[12], A. Panitch[5], C. Pascaud[28], G.D. Patel[20], H. Pawletta[2], E. Peppel[36], E. Perez[10], J.P. Phillips[20], A. Pieuchot[24], D. Pitzl[37], G. Pope[8], S. Prell[12], R. Prosi[12], K. Rabbertz[1], G. Rädel[12], F. Raupach[1], P. Reimer[31], S. Reinshagen[12], H. Rick[9], V. Riech[13], J. Riedlberger[37], F. Riepenhausen[2], S. Riess[14], E. Rizvi[21], S.M. Robertson[4],

P. Robmann[38], H.E. Roloff[† 36], R. Roosen[5], K. Rosenbauer[1], A. Rostovtsev[25], F. Rouse[8], C. Royon[10], K. Rüter[27], S. Rusakov[26], K. Rybicki[7], N. Sahlmann[2], D.P.C. Sankey[6], P. Schacht[27], S. Schiek[14], S. Schleif[16], P. Schleper[15], W. von Schlippe[21], D. Schmidt[35], G. Schmidt[14], A. Schöning[12], V. Schröder[12], E. Schuhmann[27], B. Schwab[15], F. Sefkow[12], M. Seidel[13], R. Sell[12], A. Semenov[25], V. Shekelyan[12], I. Sheviakov[26], L.N. Shtarkov[26], G. Siegmon[17], U. Siewert[17], Y. Sirois[29], I.O. Skillicorn[11], P. Smirnov[26], J.R. Smith[8], V. Solochenko[25], Y. Soloviev[26], A. Specka[29], J. Spiekermann[9], S. Spielman[29], H. Spitzer[14], F. Squinabol[28], R. Starosta[1], M. Steenbock[14], P. Steffen[12], R. Steinberg[2], H. Steiner[12,40], B. Stella[33], A. Stellberger[16], J. Stier[12], J. Stiewe[16], U. Stößlein[36], K. Stolze[36], U. Straumann[38], W. Struczinski[2], J.P. Sutton[4], S. Tapprogge[16], M. Taševský[32], V. Tchernyshov[25], S. Tchetchelnitski[25], J. Theissen[2], C. Thiebaux[29], G. Thompson[21], P. Truöl[38], J. Turnau[7], J. Tutas[15], P. Uelkes[2], A. Usik[26], S. Valkár[32], A. Valkárová[32], C. Vallée[24], D. Vandenplas[29], P. Van Esch[5], P. Van Mechelen[5], Y. Vazdik[26], P. Verrecchia[10], G. Villet[10], K. Wacker[9], A. Wagener[2], M. Wagener[34], A. Walther[9], B. Waugh[23], G. Weber[14], M. Weber[12], D. Wegener[9], A. Wegner[27], T. Wengler[15], M. Werner[15], L.R. West[4], T. Wilksen[12], S. Willard[8], M. Winde[36], G.-G. Winter[12], C. Wittek[14], E. Wünsch[12], J. Žáček[32], D. Zarbock[13], Z. Zhang[28], A. Zhokin[25], M. Zimmer[12], F. Zomer[28], J. Zsembery[10], K. Zuber[16] and M. zurNedden[38]

[1] I. Physikalisches Institut der RWTH, Aachen, Germany[a]
[2] III. Physikalisches Institut der RWTH, Aachen, Germany[a]
[3] Institut für Physik, Humboldt-Universität, Berlin, Germany[a]
[4] School of Physics and Space Research, University of Birmingham, Birmingham, UK[b]
[5] Inter-University Institute for High Energies ULB-VUB, Brussels; Universitaire Instelling Antwerpen, Wilrijk; Belgium[c]
[6] Rutherford Appleton Laboratory, Chilton, Didcot, UK[b]
[7] Institute for Nuclear Physics, Cracow, Poland[d]
[8] Physics Department and IIRPA, University of California, Davis, California, USA[e]
[9] Institut für Physik, Universität Dortmund, Dortmund, Germany[a]
[10] CEA, DSM/DAPNIA, CE-Saclay, Gif-sur-Yvette, France
[11] Department of Physics and Astronomy, University of Glasgow, Glasgow, UK[b]
[12] DESY, Hamburg, Germany[a]
[13] I. Institut für Experimentalphysik, Universität Hamburg, Hamburg, Germany[a]
[14] II. Institut für Experimentalphysik, Universität Hamburg, Hamburg, Germany[a]
[15] Physikalisches Institut, Universität Heidelberg, Heidelberg, Germany[a]
[16] Institut für Hochenergiephysik, Universität Heidelberg, Heidelberg, Germany[a]
[17] Institut für Reine und Angewandte Kernphysik, Universität Kiel, Kiel, Germany[a]
[18] Institute of Experimental Physics, Slovak Academy of Sciences, Košice, Slovak Republic[f]
[19] School of Physics and Chemistry, University of Lancaster, Lancaster, UK[b]
[20] Department of Physics, University of Liverpool, Liverpool, UK[b]
[21] Queen Mary and Westfield College, London, UK[b]
[22] Physics Department, University of Lund, Lund, Sweden[g]
[23] Physics Department, University of Manchester, Manchester, UK[b]
[24] CPPM, Université d'Aix-Marseille II, IN2P3-CNRS, Marseille, France
[25] Institute for Theoretical and Experimental Physics, Moscow, Russia
[26] Lebedev Physical Institute, Moscow, Russia[f]
[27] Max-Planck-Institut für Physik, München, Germany[a]
[28] LAL, Université de Paris-Sud, IN2P3-CNRS, Orsay, France
[29] LPNHE, Ecole Polytechnique, IN2P3-CNRS, Palaiseau, France
[30] LPNHE, Universités Paris VI and VII, IN2P3-CNRS, Paris, France

[31] Institute of Physics, Czech Academy of Sciences, Praha, Czech Republic[f,h]
[32] Nuclear Center, Charles University, Praha, Czech Republic[f,h]
[33] INFN Roma and Dipartimento di Fisica, Universita "La Sapienza", Roma, Italy
[34] Paul Scherrer Institut, Villigen, Switzerland
[35] Fachbereich Physik, Bergische Universität Gesamthochschule Wuppertal, Wuppertal, Germany[a]
[36] DESY, Institut für Hochenergiephysik, Zeuthen, Germany[a]
[37] Institut für Teilchenphysik, ETH, Zürich, Switzerland[i]
[38] Physik-Institut der Universität Zürich, Zürich, Switzerland[i]
[39] Visitor from Yerevan Phys. Inst., Armenia
[40] On leave from LBL, Berkeley, USA
[†] Deceased

[a] Supported by the Bundesministerium für Bildung, Wissenschaft, Forschung und Technologie, FRG, under contract numbers 6AC17P, 6AC47P, 6DO57I, 6HH17P, 6HH27I, 6HD17I, 6HD27I, 6KI17P, 6MP17I, and 6WT87P
[b] Supported by the UK Particle Physics and Astronomy Research Council, and formerly by the UK Science and Engineering Research Council
[c] Supported by FNRS-NFWO, IISN-IIKW
[d] Supported by the Polish State Committee for Scientific Research, grant nos. 115/E-743/SPUB/P03/109/95 and 2 P03B 244 08p01, and Stiftung für Deutsch-Polnische Zusammenarbeit, project no.506/92
[e] Supported in part by USDOE grant DE F603 91ER40674
[f] Supported by the Deutsche Forschungsgemeinschaft
[g] Supported by the Swedish Natural Science Research Council
[h] Supported by GA ČR, grant no. 202/93/2423, GA AV ČR, grant no. 19095 and GA UK, grant no. 342
[i] Supported by the Swiss National Science Foundation

1 Introduction

A prime task of the electron-proton collider HERA is the investigation of the structure of the proton. Measurements of the inclusive lepton-proton scattering cross section have been crucial for the understanding of proton substructure [1]. Early electron-proton scattering experiments have discovered pointlike proton constituents by observing a scale invariant dependence of the proton structure function $F_2(x, Q^2)$ on the four-momentum transfer squared Q^2 at Bjorken $x \geq 0.1$ and Q^2 values of about 5 GeV^2. Subsequent neutrino scattering experiments have established the Quark Parton Model (QPM) as a valid picture of the valence and sea quarks as constituents of the proton. The interaction of these partons as mediated by gluons is successfully described by Quantum Chromodynamics (QCD) which has been tested with high precision in muon-nucleon deep-inelastic scattering (DIS) experiments. Experiments at HERA extend the previously accessible kinematic range up to very large squared momentum transfers, $Q^2 > 10^3$ GeV^2, and down to very small values of Bjorken $x < 10^{-4}$.

The first measurements of the structure function $F_2(x, Q^2)$ reported at HERA, based on data collected in 1992, revealed its strong rise at low $x < 10^{-2}$ with decreasing x [2, 3]. This rise was confirmed with the more precise data of 1993 [4, 5], based on an order of magnitude increase in statistics. Such a behaviour is qualitatively expected in the asymptotic limit of Quantum Chromodynamics [6]. It is, however, not clear whether the rise of F_2 is fully described by the linear QCD evolution equations, such as the conventional DGLAP evolution [7] in $\log Q^2$ or by the BFKL evolution [8] in $\log(1/x)$, or whether there is a significant effect due to non-linear parton recombination [9]. Furthermore, it is also unclear whether this rise will persist at low values of Q^2 of the order of one GeV^2. For example, Regge inspired models expect F_2 to be rather flat as function of x at small Q^2. The quantitative investigation of the quark-gluon interaction dynamics at low x is one of the major challenges at HERA. It requires high precision for the F_2 measurement and complementary investigations of the characteristics of the hadronic final state [10].

In this paper an analysis is presented of inclusive deep-inelastic scattering data taken by the H1 collaboration in 1994 with an integrated luminosity of 2.7 pb^{-1}, which is an order of magnitude larger than in 1993. The incident electron[1] energy E_e was 27.5 GeV and the proton energy E_p was 820 GeV. The accessible kinematic range has been extended to the very high Q^2 region and the structure function F_2 has been investigated at a new level of precision. To reach lower Q^2 values and correspondingly lower x values, special samples were analysed of events with shifted interaction vertex, and of events with tagged initial state photon radiation.

This paper is organized as follows. After a short introduction to the kinematics of inclusive ep scattering (section 2), the H1 apparatus is briefly sketched (section 3). The different 1994 data samples, the luminosity determination and the Monte Carlo simulation are described in section 4. Next the event selection including the background rejection (section 5) is discussed for the different data samples used. Section 6 describes the F_2 analyses. In section 7 the results are discussed. A phenomenological analysis of F_2 is performed and the data are compared to recent model calculations at low Q^2. The data are also studied in the framework of perturbative QCD and the gluon distribution is extracted. The paper is summarized in section 8.

[1]HERA operated with e^-p collisions in 1992, 1993 and the start of 1994, and e^+p collisions for the major part of 1994. In this paper the incident and scattered lepton will always be referred to as an "electron".

2 Kinematics

The structure function $F_2(x, Q^2)$ is derived from the inclusive electron-proton scattering cross section. It depends on the squared four-momentum transfer Q^2 and the scaling variable x. These variables are related to the inelasticity parameter y and to the total squared centre of mass energy of the collision s since $Q^2 = xys$ with $s = 4E_eE_p$. A salient feature of the HERA collider experiments is the possibility of measuring not only the scattered electron but also the complete hadronic final state, apart from losses near the beam pipe. This means that the kinematic variables x, y and Q^2 can be determined with complementary methods which are sensitive to different systematic effects. These methods were exploited and detailed already in [4] which describes the analysis of the 1993 data. An appropriate combination of the results ensures maximum coverage of the available kinematic range.

The methods used in the analysis of the 1994 data are the so called "E" (electron) method using only the information of the scattered electron and the so called "Σ" method calculating the kinematics based on both the scattered electron and the hadronic final state measurements [11]. The E method, which is independent of the hadronic final state, apart from the requirement that the interaction vertex is reconstructed using the final state hadrons, has at large y the best resolution in x and Q^2 but needs sizeable radiative corrections. At low y the E method is not applied due to the degradation of the y_e resolution as $1/y$. The Σ method, which has small radiative corrections, relies mostly on the hadronic measurement which has still an acceptable resolution at low y values and can be used from very low to large y values. The E and Σ results were compared in order to control the calculation of the systematic errors. The basic formulae for Q^2 and y for the E method are:

$$y_e = 1 - \frac{E'_e}{E_e}\sin^2\frac{\theta_e}{2} \qquad\qquad Q^2_e = 4E'_eE_e\cos^2\frac{\theta_e}{2} = \frac{E'^2_e\sin^2\theta_e}{1-y_e} \tag{1}$$

where E'_e and θ_e are the energy and polar angle of the scattered electron. The polar angle θ_e is defined with respect to the proton beam or z direction, termed "forward" region. The formulae for the Σ method are

$$y_\Sigma = \frac{\Sigma}{\Sigma + E'_e(1-\cos\theta_e)} \qquad\qquad Q^2_\Sigma = \frac{E'^2_e\sin^2\theta_e}{1-y_\Sigma} \tag{2}$$

with

$$\Sigma = \sum_h (E_h - p_{z,h}). \tag{3}$$

Here E_h and $p_{z,h}$ are the energy and longitudinal momentum component of a particle h, the summation is over all hadronic final state particles and the masses are neglected. The denominator of y_Σ is equal to $2E_e$ but measured with all secondary particles. Thus

$$y_\Sigma = \frac{y_h}{1 + y_h - y_e} \tag{4}$$

with the standard definition

$$y_h = \frac{\Sigma}{2E_e}. \tag{5}$$

The variable x is calculated as $x = Q^2/ys$.

3 The H1 Detector

The H1 detector [12] is a nearly hermetic multi-purpose apparatus built to investigate the inelastic high-energy interactions of electrons and protons at HERA. The structure function measurement relies essentially on the inner tracking chamber system and on the backward electromagnetic and the liquid argon calorimeters which will be described here briefly.

The tracking system includes the central tracking chambers, the forward tracker modules and a backward proportional chamber. These chambers are placed around the beam pipe at z positions between -1.5 and 2.5 m. A superconducting solenoid surrounding both the tracking system and the liquid argon calorimeter provides a uniform magnetic field of 1.15 T.

The central jet chamber (CJC) consists of two concentric drift chambers covering a polar angle range from 15^o to 165^o. Tracks crossing the CJC are measured with a transverse momentum resolution of $\delta p_T/p_T < 0.01 \cdot p_T/\mathrm{GeV}$. The CJC is supplemented by two cylindrical drift chambers at radii of 18 and 47 cm, respectively, to improve the determination of the z coordinate of the tracks. A proportional chamber is attached to each of the z drift chambers for triggering.

A tracking chamber system made of three identical modules measures hadrons emitted in the forward direction (7^o to 20^o). The forward tracker (FT) is used to determine the vertex for the events which leave no track in the CJC. This allows an extension of the analysis to larger x values.

In the backward region, attached to the backward electromagnetic calorimeter (BEMC), a four plane multiwire proportional chamber (BPC) was located with a polar angle acceptance of 151^o to 174.5^o. The BPC provides a space point for charged particles entering the BEMC which is used for low $Q^2 \leq 120$ GeV^2 events to identify electrons and to measure θ_e. The spatial resolution for reconstructed BPC hits is about 1.5 mm in the plane perpendicular to the beam axis.

The backward electromagnetic calorimeter [13] which detects the scattered electron at low Q^2 is made of 88 lead/scintillator stacks with a size of 16×16 cm^2 and a depth of 22 radiation lengths corresponding to about one interaction length. Around the beampipe the stacks are of triangular shape. The angular coverage of the BEMC is $155^o < \theta_e < 176^o$. A 1.5 cm spatial resolution of the lateral shower position is achieved using four photodiodes which detect the wavelength shifted light from each of the scintillator stacks. A scintillator hodoscope (TOF) situated behind the BEMC is used to veto proton-induced background events based on their early time of arrival compared with nominal ep collisions.

Hadronic final state energies and the scattered electron at high Q^2 ($Q^2 \geq 120$ GeV^2) are measured in the liquid argon (LAR) calorimeter [14] which covers an angular region between 3^o and 155^o. The calorimeter consists of an electromagnetic section with lead absorber plates and a hadronic section with stainless steel absorber plates. Both sections are highly segmented in the transverse and longitudinal directions with about 44000 cells in total. The electromagnetic part has a depth between 20 and 30 radiation lengths. The total depth of both calorimeters varies between 4.5 and 8 interaction lengths.

The luminosity was determined from the measured cross section of the Bethe Heitler (BH) reaction $ep \to ep\gamma$. The final state electron and photon can be detected in calorimeters (electron and photon "taggers") close to the beam pipe but at large distances from the main detector (at $z = -33$ m and $z = -103$ m).

4 Data and Monte Carlo Samples

4.1 Data Samples

Several data samples have been analysed in order to cover maximally the kinematic plane. The distribution of the events is shown in Fig. 1. The majority of the events are produced with the interaction vertex centered around zero in z, called the "nominal vertex" sample (shown as regions C and D in Fig. 1). Throughout this paper, the low (high) Q^2 sample refers to events in which the scattered electron has been detected in the BEMC (LAr calorimeter). To reduce the systematic errors of the F_2 measurement, a strict data selection was performed based on the behaviour of the main detector components. This behaviour was required to be optimal for the low Q^2 analysis of the nominal vertex sample which allows the highest precision to be reached. The remaining integrated luminosity for the low Q^2 sample is 2.2 pb^{-1}, the one for the high Q^2 sample is 2.7 pb^{-1}. The number of accepted events per unit luminosity was checked to be constant within statistical errors during the data taking period.

In order to study the behaviour of F_2 at small Q^2 several means were used to extend the acceptance to this kinematic region using special event samples. For DIS events at very low Q^2 the electron is scattered through a large angle θ_e. For θ_e values greater than 173^0 and the interaction vertex at its nominal position at $z = +3$ cm the electron hits the inner edge of the BEMC calorimeter or remains undetected near the beam pipe. The acceptance extension in the backward region was realized as follows:

- During good accelerator background conditions, the innermost parts of the backward electromagnetic calorimeter (BEMC) around the beampipe were included in the trigger for part of the time. Since these detector elements are of triangular shape, these data will be referred to as the "open triangle" data sample. An integrated luminosity of 0.27 pb^{-1} was accumulated. The kinematic region covered by this sample is shown as region (B) in Fig. 1.

- As in 1993 [4], the interaction point was shifted in the forward direction to an average position of $z = +67$ cm which permits measurements up to $\theta_e \simeq 176.5^o$. This sample of 58 nb^{-1} of data is referred to as the "shifted vertex" data sample to distinguish it from the data with a nominal event vertex. It covers region (A) in Fig. 1.

- The low Q^2 region was also accessed by analyzing events from the so called early proton satellite bunch colliding with an electron bunch at $z \simeq +68$ cm. The kinematic region covered by this sample is similar to that of the shifted vertex data sample. The "satellite" data sample amounts to $\simeq 3\%$ of the total data corresponding to a total "luminosity" of 68 nb^{-1} selected over the whole run period.

- Finally, a sample of deep-inelastic radiative events was extracted with a hard photon emitted collinear with the incident electron. These events have a reduced incident electron beam energy which allows access to very low Q^2 values with the present detector setup. Since only about 2% of the DIS events are tagged as radiative events, the nominal vertex sample had to be used for this study. Subsequently the tagged radiative events are referred to as "the radiative event sample" and the bulk of the data are sometimes called "non-radiative" in contrast.

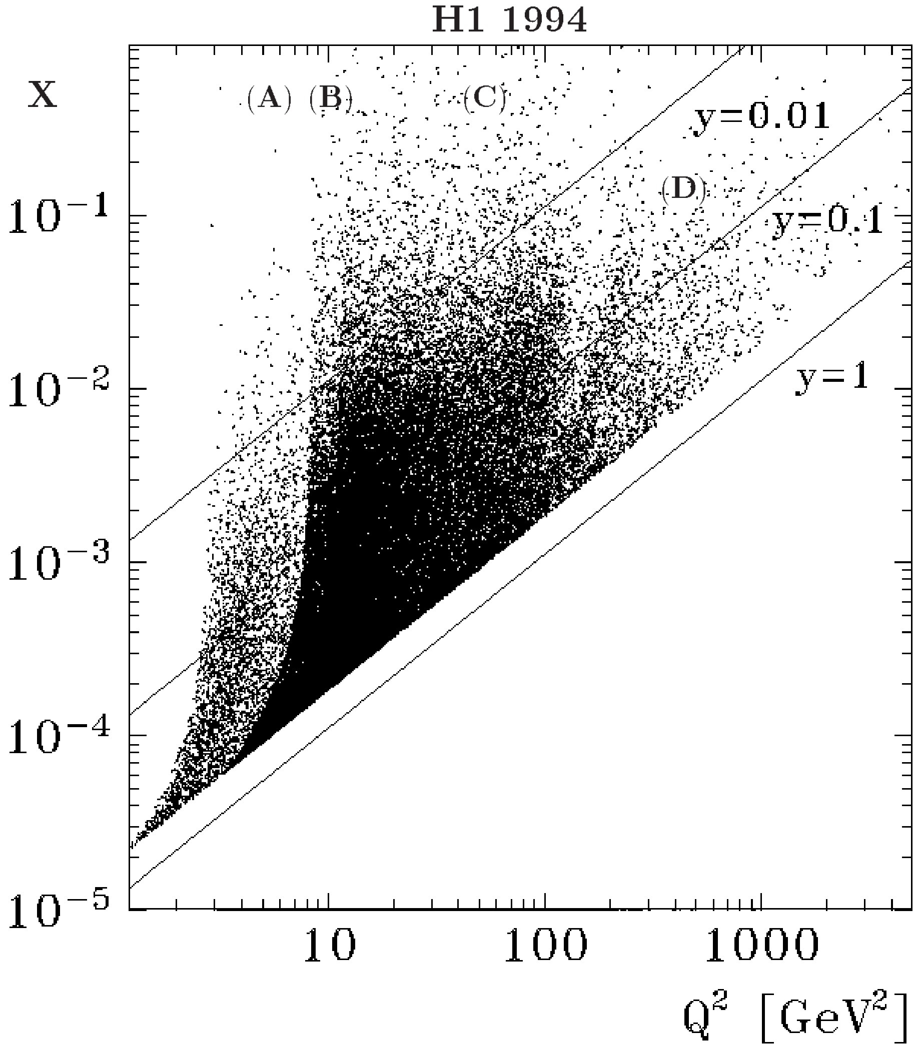

Figure 1: *Distribution of the event sample in the (x, Q^2) plane. The 4 visible regions (A,B,C,D) correspond to A) events recorded during a period in which the interaction region was shifted with respect to the nominal position allowing access to larger θ_e; B) events from the nominal vertex position taken in a period in which the innermost BEMC stacks of triangular shape were included in the trigger ("opened triangles", see text) or C) not included; D) high Q^2 events with the scattered electron detected in the LAr calorimeter.*

4.2 Luminosity Determination

The most precise method of determining the luminosity from the reaction $ep \to ep\gamma$ is based on the measurement of the energy spectrum of hard photons ($E_\gamma > 10$ GeV) as explained in [15] for the 1993 data. The main uncertainties of the measurement of the integrated luminosity for the 1994 nominal vertex data are: the photon tagger absolute energy scale (0.9%), the trigger efficiency of the luminosity system (0.3%), the precision of the electron gas background subtraction (0.4%), the photon-tagger acceptance (0.5%), multiple photon overlaps (0.4%), the precision of integration resulting from the 10 sec interval between consecutive luminosity measurements (0.5%) and the correction for satellite bunches (0.5%). Major improvements with respect to 1993 data include the trigger efficiency, the satellite bunch correction and the precision of the energy scale in the photon tagger. The precision of the luminosity measurement for the nominal vertex data sample is 1.5% which represents an improvement of a factor of 3 with respect to the 1993 data analysis. For the shifted vertex data sample the luminosity uncertainty is 3.9%.

The results of this measurement were checked for consistency with a sample of Bethe Heitler events in which both the electron and photon are detected simultaneously, and with QED Compton events. Both these analyses are subject to different systematics, compared with the hard photon method, allowing a cross check of the luminosity with a precision of up to 6%.

The integrated luminosity of the satellite data sample was obtained from the measured integrated luminosity for the shifted vertex data multiplied by the efficiency corrected event ratio in a kinematic region common to both data sets. The precision of that luminosity determination was estimated to be 7.1%.

4.3 Monte Carlo Simulation

More than one million Monte Carlo DIS events were generated using the DJANGO [16] program. The Monte Carlo event statistics correspond to an integrated luminosity of approximately 18 pb^{-1}. The DJANGO program is based on HERACLES [17] for the electroweak interaction and on the LEPTO program [18] to simulate the hadronic final state. HERACLES includes first order radiative corrections, the simulation of real Bremsstrahlung photons and the longitudinal structure function. The acceptance corrections were performed using the GRV parametrization [19] which describes rather well the HERA F_2 results based on the 1993 data. LEPTO uses the colour dipole model (CDM) as implemented in ARIADNE [20] which is in good agreement with data on the energy flow and other characteristics of the final state as measured by H1 [21] and ZEUS [22]. For the determination of systematic errors connected with the topology of the hadronic final state, the HERWIG model [23] was used.

Photoproduction background was simulated based on the PHOJET [24], PYTHIA [25] and RAYVDM [26] generators for γp interactions. With these models large samples of photoproduction events were generated which contained all classes of events (elastic, soft hadronic collisions, hard scattering processes and heavy flavour production).

It was found that about 10% of the DIS data at HERA consists of events with a large gap in pseudo-rapidity around the proton remnant direction [27]. These events were found to be compatible with diffractive exchange and are well described by the model RAPGAP [28] as deep-inelastic scattering on a colourless object –termed a pomeron– emitted from the proton. The hadronic final state of these events is also well described by RAPGAP which includes ARIADNE for QCD effects. The RAPGAP Monte Carlo simulation was used to check the effect of the large rapidity gap events on the vertex reconstruction efficiency which depends mostly on the final state topology of the events. Differences between rapidity gap and "standard" DIS events of up to 2% were found at large $y > 0.4$ and smaller at low y, and were included in the systematic error of F_2.

For the events generated with the models described above the detector response was simulated in detail [12] using a program based on GEANT [29]. The simulated Monte Carlo events were subjected to the same reconstruction and analysis chain as the real data.

5 Event Selection

The low Q^2 DIS events in the backward region were triggered by an energy cluster in the BEMC ($E'_e > 4$ GeV) which was not vetoed by the TOF. The high Q^2 events were triggered by requiring an electromagnetic energy cluster in the LAr calorimeter ($E'_e > 8$ GeV). A trigger of lower energy threshold ($E'_e > 6$ GeV) also accepted the event if there was simultaneously a tracking trigger. In the region of the final F_2 data presented below the trigger efficiency, which has been determined from the data, is about 80% for $E'_e \sim 8$ GeV, and becomes larger than 99% for $E'_e > 10$ GeV.

5.1 Selection of Deep-Inelastic Scattering Events

Deep-inelastic scattering events in H1 are identified by the detection of the scattered electron in the BEMC or LAr calorimeter and the presence of a reconstructed interaction vertex. The electron identification cuts, fiducial volume and vertex requirement are detailed in Table 1.

These selection criteria follow closely those of the 1993 data analysis [4]. For the low Q^2 nominal vertex sample ($Q^2 \leq 120$ GeV^2) an additional cut $r_{BPC} < 64$ cm is applied, where r_{BPC} is the radial distance of the electron hit in the BPC to the beam axis. This cut prevents the electron from entering the transition region between the BEMC and the LAr calorimeter where the energy corrections are large and depend strongly on the impact point. For the same reason, the high Q^2 events ($Q^2 > 120$ GeV^2) are accepted only if the electron cluster is fully contained in the LAr calorimeter. Despite these conditions, the measurement could also be performed for intermediate Q^2 ($Q^2 \sim 120$ GeV^2) due to the ± 30 cm spread of the event vertex position around its nominal position.

The scattered electron is identified with the electromagnetic cluster of maximum energy which satisfies the estimator cuts of Table 1. The electron identification efficiency, determined from Monte Carlo simulation studies, is better than 97% except at $Q^2 \leq 6.5$ GeV^2 where it falls to 94% at the lowest x values.

At low Q^2 the main sources of non-ep background are due to proton beam interactions with residual gas and beam line elements upstream of the H1 detector. At high Q^2 the main background is due to cosmic ray events and muons travelling off axis parallel to the proton beam. An efficient reduction of these background contributions is provided by the minimum

	low Q^2 (shifted vtx)	low Q^2 (nominal vtx)	high Q^2	
	E, Σ method	E, Σ method	E method	Σ method
$\theta_e/^o$	≤ 176	< 173	< 150	≤ 153
E'_e/GeV	> 11	> 11	> 11	> 11
z_{vertex}/cm	67$\pm$ 30	5$\pm$ 30	5$\pm$ 30	5$\pm$ 30
electron identif.	$\epsilon_1 < 5$ cm	$\epsilon_1 < 5$ cm	$\epsilon_3 > 50\%$	$\epsilon_3 > 65\%$
electron identif.	$\epsilon_2 < 5$ cm	$\epsilon_2 < 5$ cm	$\epsilon_4 > 3\%$	$\epsilon_5 < 30$ mrad

Table 1: *Summary of event selection criteria for the shifted and the nominal vertex (vtx) data at low and high Q^2. The approximate event numbers are 10000, 220000 and 9000 events respectively. For the open triangle data sample the θ_e cut is 174°. For the electron identification several estimators were used: ϵ_1: electron cluster radius; ϵ_2: smallest distance from the closest hit in the BPC to the centroid of the electron cluster; ϵ_3: fraction of the electron energy deposited in the 4 most energetic cells of the cluster; ϵ_4: fraction of the electron energy deposited in the first 3 radiation lengths of the calorimeter; ϵ_5: angle between the line connecting the vertex to the centroid of the electron cluster and the associated track.*

energy and the vertex requirements discussed above. The number of residual beam-induced background events was estimated from non-colliding bunch studies, and the number of cosmic events from scanning. Both together represent less than 1% of the number of selected events in any (x, Q^2) bin.

The only significant background to DIS from ep interactions is due to photoproduction events where the scattered electron escapes the detector along the beam pipe but in which an energy cluster from the hadronic final state fakes a scattered electron. About 10% of these events are identified as photoproduction background if the scattered electron is found in the electron tagger. Photoproduction events were simulated to estimate this background. The photoproduction background was subtracted statistically bin by bin. Only 12 bins, out of a total of 193 (x, Q^2) bins, have a contamination larger than 3%. This contamination never exceeds 15% in any bin.

Figure 2a shows the distribution of the angle of the scattered electron for the shifted vertex data compared to the Monte Carlo simulation weighted with the measured structure function (see section 6). The Monte Carlo simulation is normalized to the luminosity and agrees well with the data illustrating the level of residual background in the low Q^2 sample. In Fig. 2b the normalized energy spectrum in the electron tagger is shown which is reproduced by the background photoproduction event simulation.

Figure 3a shows the distribution of the energy of the scattered electron for the high statistics nominal vertex data. The simulation gives an excellent description of the data from the low energy up to the so called kinematic peak region, i.e. the region around the value of the incident electron beam energy. This agreement was achieved after a spatially dependent calibration of the data and Monte Carlo response [30] using the double-angle method [31]. The small remaining contribution of the photoproduction background is also shown. In Fig. 3b the fractions of y_h originating from tracks, BEMC and LAr calorimeter are given as a function of $\log_{10} y_h$. In this analysis the y_h variable is determined by using a combination of central tracks and calorimeter cells [32]. An isolation criterion is used to avoid counting the energy of the LAr cells originating from a track already used in y_h. For y <0.15, i.e. in the region where the Σ method will be used for the F_2 result, the measurement is dominated

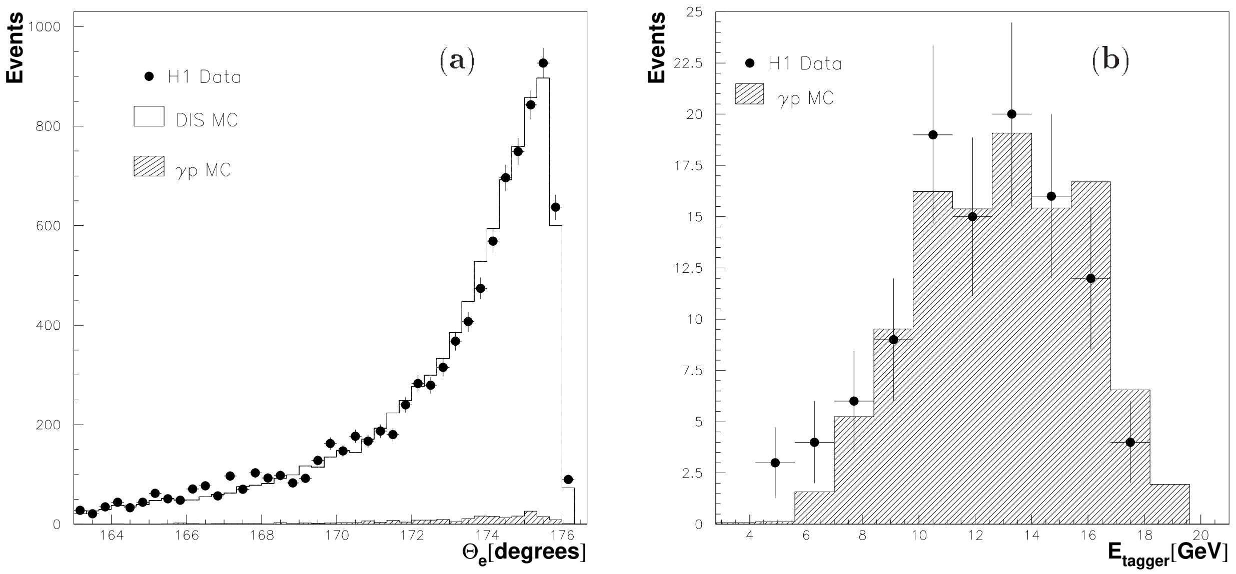

Figure 2: *Shifted vertex data: experimental and Monte Carlo distributions of a) the polar angle of the scattered electron and b) the energy of the scattered electron in photoproduction background events detected in the electron tagger.*

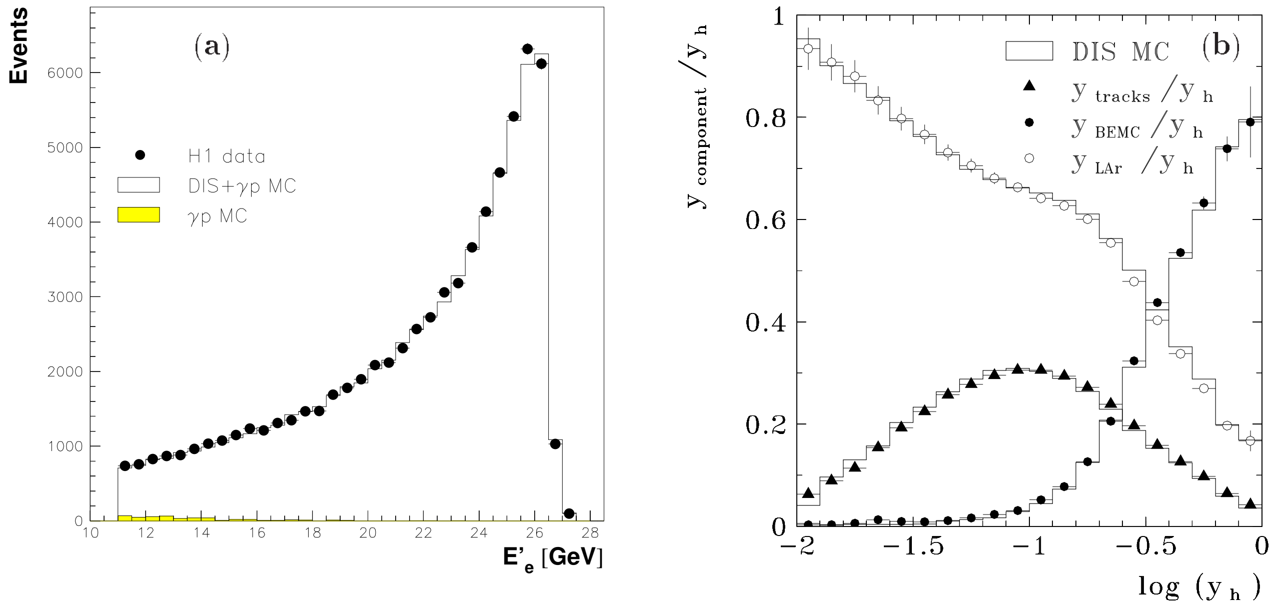

Figure 3: *Nominal vertex data with the scattered electron in the BEMC ($Q^2 \leq 120$ GeV^2): experimental and Monte Carlo distributions a) of the scattered electron energy and b) of the fraction of y_h contributed by the tracks, the LAr calorimeter and the BEMC.*

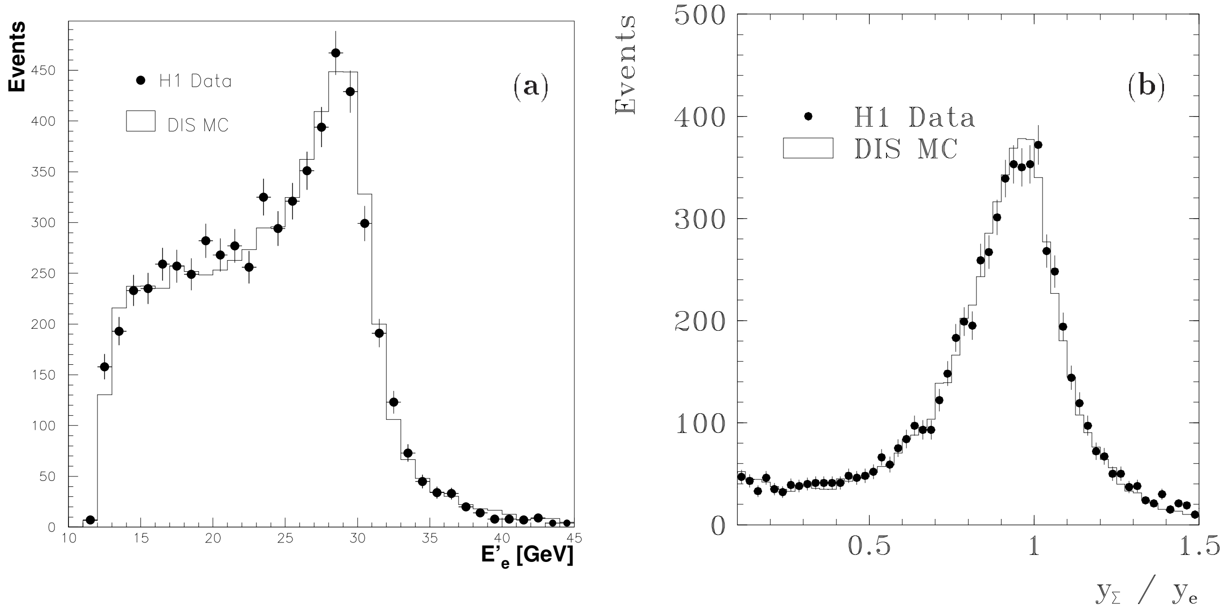

Figure 4: *High Q^2 data: experimental and Monte Carlo distributions a) of the energy of the scattered electron detected in the LAr calorimeter and b) of the ratio y_Σ/y_e, for $y_e \geq 0.05$.*

by the track reconstruction and the LAr measurement (Fig. 3b). At larger y, the BEMC contribution plays an increasing role due to the low energy particles which accumulate in the backward direction. The DIS Monte Carlo simulation describes well these fractions in the complete kinematic range.

Figure 4a shows the distribution of the energy of the scattered electron detected in the LAr calorimeter. It is well described by the Monte Carlo simulation. A detailed calibration was carried out by comparing events from the kinematic peak at low y (< 0.1) with simulation, including corrections for the energy lost due to the dead material between the wheels which make up the LAr calorimeter [33]. This procedure has been cross checked with the double-angle method.

Figure 4b shows the ratio y_Σ/y_e in the high Q^2 sample compared to the Monte Carlo expectation. The resolution of this ratio, which is calculated for $y_e > 0.05$, and thus of y_Σ is better than 13% in this kinematic region. The "tail" visible at values below 0.7 is due to radiative events, and is well described by the Monte Carlo simulation.

5.2 Selection of Deep-Inelastic Radiative Events

A sample of deep-inelastic events with an energetic photon ($E_\gamma > 4$ GeV) emitted collinear with the incident electron was selected. These radiative events can be interpreted as deep-

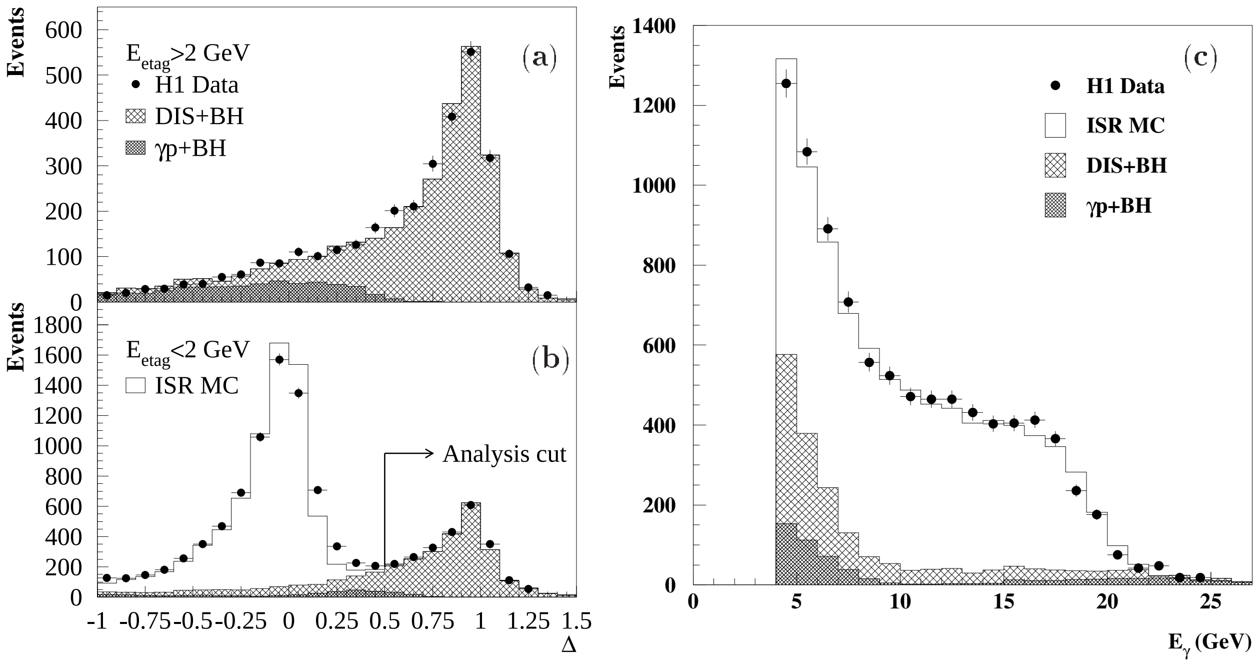

Figure 5: *Radiative events: experimental and Monte Carlo distributions of Δ (eq. 6) with a) the energy detected in the electron tagger (E_{etag}) bigger than 2 GeV; b) with $E_{etag} < 2$ GeV and c) distribution of the photon energy detected in the photon tagger. The analysis cut in b) indicates the region of $\Delta >$ 0.5 excluded from the analysis. The full solid line in b) and c) represents the sum of all three contributions in the Monte Carlo: DIS initial state radiation events (ISR MC), DIS events with a BH overlap (DIS + BH) and photoproduction events with a BH overlap (γp + BH).*

inelastic scattering events with a reduced ("true") incident energy $E_t = E_e - E_\gamma$ which can be reconstructed due to the additional detection of the radiated photon in the small angle photon tagger of the luminosity system. When using the E method, the kinematic variables y_t and Q_t^2 are obtained by replacing in eq.1 the nominal beam energy by the reduced energy E_t. Note that Q_Σ^2 and y_Σ are unchanged by the $E_e \to E_t$ transformation while x_Σ is affected.

A first experimental study of this process at HERA has been published [15, 34] by the H1 collaboration using 1993 data, which where however too limited in statistics for a quantitative study of the proton structure. The larger integrated luminosity of the 1994 data permits a significant F_2 measurement for Q^2 values down to $1.5\,\mathrm{GeV}^2$. The ZEUS collaboration [36] recently published results on F_2 using this method.

A summary of the selection criteria of the final sample of about 8200 events is given in Table 2 [35]. The event selection for radiative events is similar to the one for low Q^2 non-radiative events, apart from the additional requirement of a detected photon with at least 4 GeV in the small angle photon tagger of the luminosity system. This requirement also reduces the photoproduction background. Therefore the minimum scattered electron energy can be lowered to 8 GeV.

The selected sample contains both radiative DIS events and pile–up events due to overlaps of DIS and γp events with Bethe Heitler events in a time window of ± 5 ns. The pile-up events are partly removed from the sample by requiring the energy in the electron tagger, E_{etag}, to be less than 2 GeV, but the majority of them remains.

The background can be controlled through the redundancy of the true electron beam energy measurement E_t. For radiative DIS events we expect measurements of the quantity

$$\Delta \equiv [E_\gamma - E_e(y_e - y_h)]/E_\gamma \tag{6}$$

to be concentrated around zero while for pile-up DIS events a concentration around one is expected. Here y_e and y_h are calculated according to eqs. 1 and 5. The distribution of Δ is shown in Fig. 5 for a sample of events with a) $E_{etag} > 2$ GeV (dominantly ep collisions with BH overlap events) and b) $E_{etag} < 2$ GeV. The data are compared with Monte Carlo simulation. The pile-up sample in Fig. 5a shows a clear peak for $\Delta = 1$, and is well described by the sum of simulated DIS and γp distributions with overlap of BH events. Fig. 5b shows a peak for $\Delta = 1$ from residual pile-up events for which the electron from the BH event was not detected, and a peak around $\Delta = 0$ from genuine radiative events. Radiative events are selected in this analysis by requiring $\Delta < 0.5$. The background of pile-up events as estimated by the Monte Carlo simulation studies is subtracted statistically. The remaining background from overlap γp and DIS events estimated from Monte Carlo studies amounts to 8%, with at most 15% in an x, Q^2 bin. In Fig. 5c the photon energy spectrum as measured in the photon tagger is shown for the selected sample and compared with simulated signal and background distributions. There is a good agreement between data and Monte Carlo simulation.

	low Q^2 (radiative events)
	E, Σ method
$\theta_e/^o$	≤ 174
E'_e/GeV	> 8
z_{vertex}/cm	5$\pm$ 35
electron identif.	$\epsilon_1 < 5$ cm
electron identif.	$\epsilon_2 < 4$ cm
E_γ/GeV	> 4
E_{etag}/GeV	< 2
Δ	< 0.5

Table 2: *Summary of event selection criteria for the radiative event sample. For the electron identification two estimators were used: ϵ_1: electron cluster radius and ϵ_2: smallest distance from the closest track to the centroid of the electron cluster. The variable Δ is defined in eq. 6.*

6 Structure Function Measurement

The structure function $F_2(x, Q^2)$ was derived from the one-photon exchange cross section

$$\frac{d^2\sigma}{dxdQ^2} = \frac{2\pi\alpha^2}{Q^4 x}(2 - 2y + \frac{y^2}{1+R})F_2(x, Q^2). \tag{7}$$

The structure function ratio $R = F_2/2xF_1 - 1$ has not yet been measured at HERA. It was calculated using the QCD relation [37] with the NLO strong coupling constant [38] and the

GRV structure function parametrization. Note that a 20% error on R corresponds to about 2% uncertainty on F_2 at $y = 0.6$ for R of about 0.6. The R values are quoted in Tables 7 and 8; no extra effect of the R uncertainty on F_2 was considered.

Compared to the previous H1 analysis [4] the F_2 measurement has been extended to lower and higher Q^2 (from $4.5 - 1600$ GeV^2 to $1.5 - 5000$ GeV^2), and to lower and higher x (from $1.8 \cdot 10^{-4} \leq x \leq 0.13$ to $3 \cdot 10^{-5} \leq x \leq 0.32$). The determination of the structure function requires the measured event numbers to be converted to the bin averaged cross section based on the Monte Carlo acceptance calculation. The binning in x was governed by the detector resolution and could be chosen to be rather fine since the E and Σ methods were used in the optimum range at low and high x, respectively. The x resolution is better than 20%. The Q^2 resolution is about 5% and the number of bins in Q^2 was adapted to statistics. All detector efficiencies were determined from the data utilizing the redundancy of the apparatus. Apart from very small extra corrections, all efficiencies were correctly reproduced by the Monte Carlo simulation. The bin averaged cross section was corrected for higher order QED radiative contributions using the program HECTOR [39]. Effects due to Z boson exchange at present values of Q^2 and y are smaller than 3% and were treated as part of the radiative corrections.

Different data sets are available which, for a given (Q^2, x) interval, use different parts of the detectors. Thus many cross checks could be made in kinematic regions of overlap for the two kinematic reconstruction methods and these gave very satisfactory results. In this paper results are presented from the radiative F_2 analysis ($1.5 \leq Q^2 \leq 3.5$ GeV^2), from the shifted vertex analysis ($1.5 \leq Q^2 \leq 2.5$ GeV^2), from a combination of the shifted vertex and the satellite bunch analysis ($3.5 \leq Q^2 \leq 6.5$ GeV^2), from the open triangle analysis (Q^2= 8.5 GeV^2) and from the nominal high statistics sample when the scattered electron is detected in the BEMC ($12 \leq Q^2 \leq 120$ GeV^2) or in the LAr calorimeter ($120 < Q^2 \leq 5000$ GeV^2).

Compared with the analysis of the 1993 data, many uncertainties have been reduced. The systematic errors are due to the following sources:

- The uncertainty in the electron energy scale which is 1% in the BEMC, and 3% in the LAr calorimeter. Since the y_e resolution varies as $1/y$ with the energy resolution even a 1% error on $\delta E/E$ can lead to 10% errors on F_2 at low y in the E method.
- The uncertainty in the hadronic energy scale: the detailed study of y_h/y_e and of $p_{T,h}/p_{T,e}$ (p_T is the momentum transverse to the beam axis) allowed the assignment of a 4% error on the hadronic energy deposited in the LAr calorimeter, a 15% error on the same quantity in the BEMC, and a 3% error on the y_h fraction carried by the tracks. These errors take into account the intrinsic energy scale uncertainty of each detector and the uncertainty of the sharing of the total hadronic final state energy between these three subdetectors. These numbers also include uncertainties due to the treatment of the electronic noise in the LAr calorimeter and the BEMC.
- An uncertainty of up to 1 mrad for the electron polar angle which leads to an error on F_2 of 8% at low Q^2.
- Apart from the electron identification, all efficiencies were determined from the data and compared with Monte Carlo simulation. The agreement between the experimental and the simulated values for the individual efficiencies was found to be better than

2%. An overall error of 2% was assigned due to the imperfect description of the various efficiencies. A larger error was added to account for the variation of the vertex reconstruction efficiency at large x (up to 8%) where jets get closer to the beam pipe in the forward direction, and at small x or large θ (up to 4%) where H1 had no further tracking device besides the BPC to monitor the vertex efficiency.

- Uncertainties in the hadronic corrections, the cross section extrapolation towards $Q^2 = 0$ and higher order corrections, which give an error of up to 2% in the radiative correction. The accuracy was cross checked by comparing the HECTOR calculation with the HERACLES Monte Carlo simulation results. The agreement to the few percent level between the structure function results obtained with the E and the Σ methods is an additional cross check for the control of the radiative corrections.

- The structure function dependence of the acceptance which was kept below 1% by performing a two step iterative analysis. The uncertainty in the simulation of the hadronic final state reflects most prominently in the efficiency for the requirement of an interaction vertex from tracks. A comparison of the different models (sect 4.3) for the hadronic final state was used to assign an additional 3% systematic error entering in all analyses at low x through the vertex efficiency.

- Based on the control data sample of electron tagged γp events the uncertainty due to photoproduction background could be estimated to be smaller than 30% of the correction applied. This is equivalent to at most a 5% systematic error in the highest y bins at lower Q^2 only.

- Statistical errors in the Monte Carlo acceptance and efficiency calculations were computed and added quadratically to the systematic error.

- For the analysis of radiative events an additional 1.5% uncertainty on the photon energy measurement in the photon tagger was considered and a 2% systematic error was added due to the uncertainty of the photon tagger geometrical acceptance. An uncertainty on the trigger efficiency of 6% to 9% was included for the lowest x points.

Some of the systematic uncertainties affect differently the F_2 measurement in the different methods. The systematic errors are given in Tables 7 and 8 point by point. However, some are strongly correlated over a large kinematic range. These correlations have been considered in the fits reported below. The matrix with the many different error contributions is available upon request to the H1 collaboration. In Fig. 6 the comparison of the measurements using the E and using the Σ method is shown. Both are in good agreement for all Q^2 values. Some possible discrepancies between both methods, e.g. at $Q^2 = 3.5$ GeV^2, were investigated carefully and taken into account when evaluating the systematic error of the final structure function values if they could not be resolved. Small deviations are possible though, due to the different population of the x, Q^2 plane between the methods of calculating the kinematics. The two measurements are combined using the E method for $y > 0.15$ and the Σ method for $y < 0.15$. The result is shown in Fig. 7 and given in Tables 7 and 8. The measurements obtained from the low Q^2 nominal vertex sample have a typical systematic error of 5%. The large statistics allow the measurement of F_2 to reach Q^2 values of 5000 GeV^2, and to achieve a few percent statistical precision at Q^2 below 100 GeV^2. The results are in good agreement with the previous H1 publication [4]. In particular, the distinct rise of F_2 towards low x, observed with the 1992 and 1993 [2, 4] data, is confirmed with higher precision and extends now to significantly lower Q^2 values.

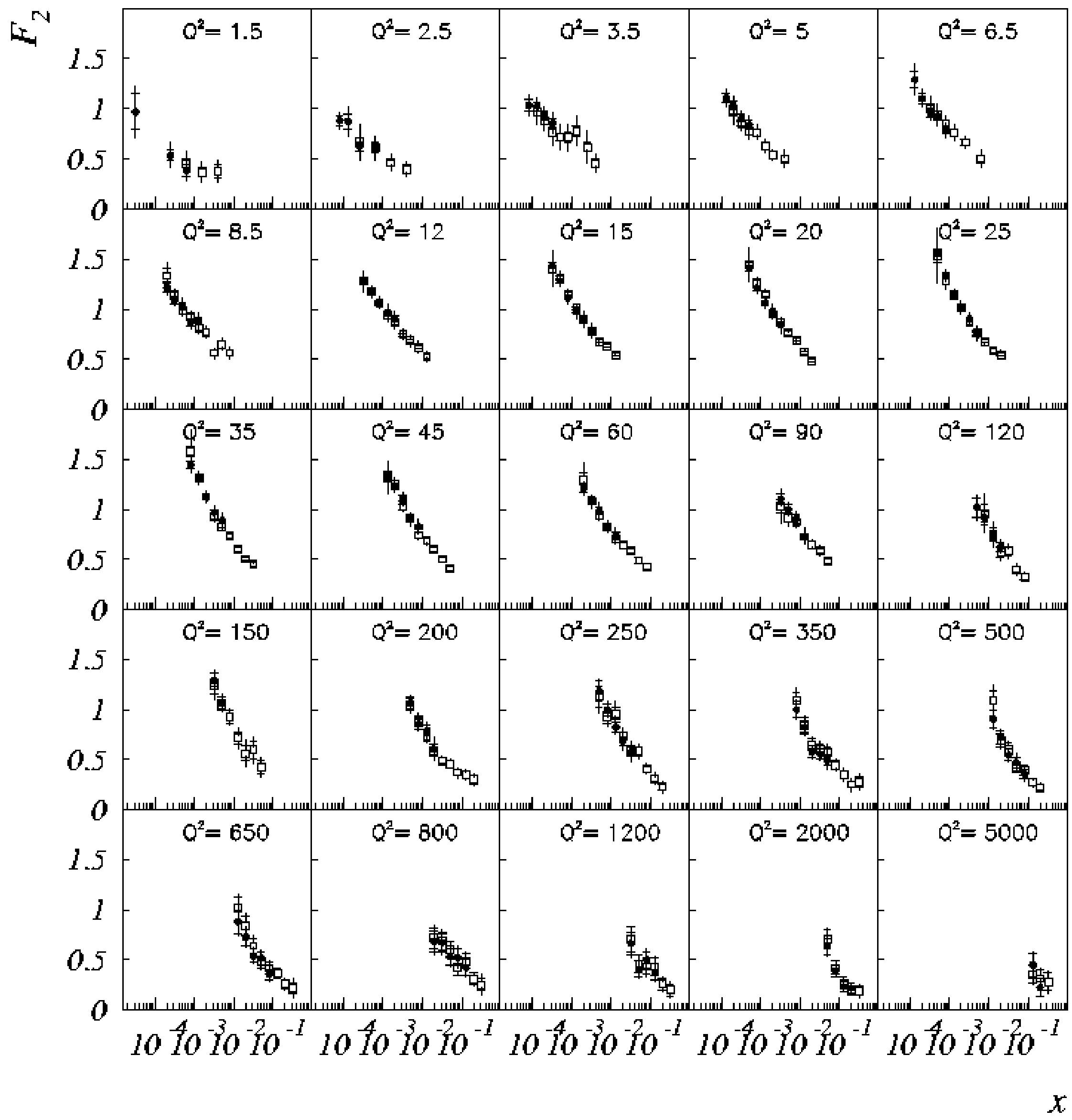

Figure 6: *Measurement of the structure function with the electron (closed circles) and the Σ method (open squares). The inner error bar is the statistical error. The full error bar represents the statistical and systematic errors added in quadrature disregarding the error from the luminosity measurement.*

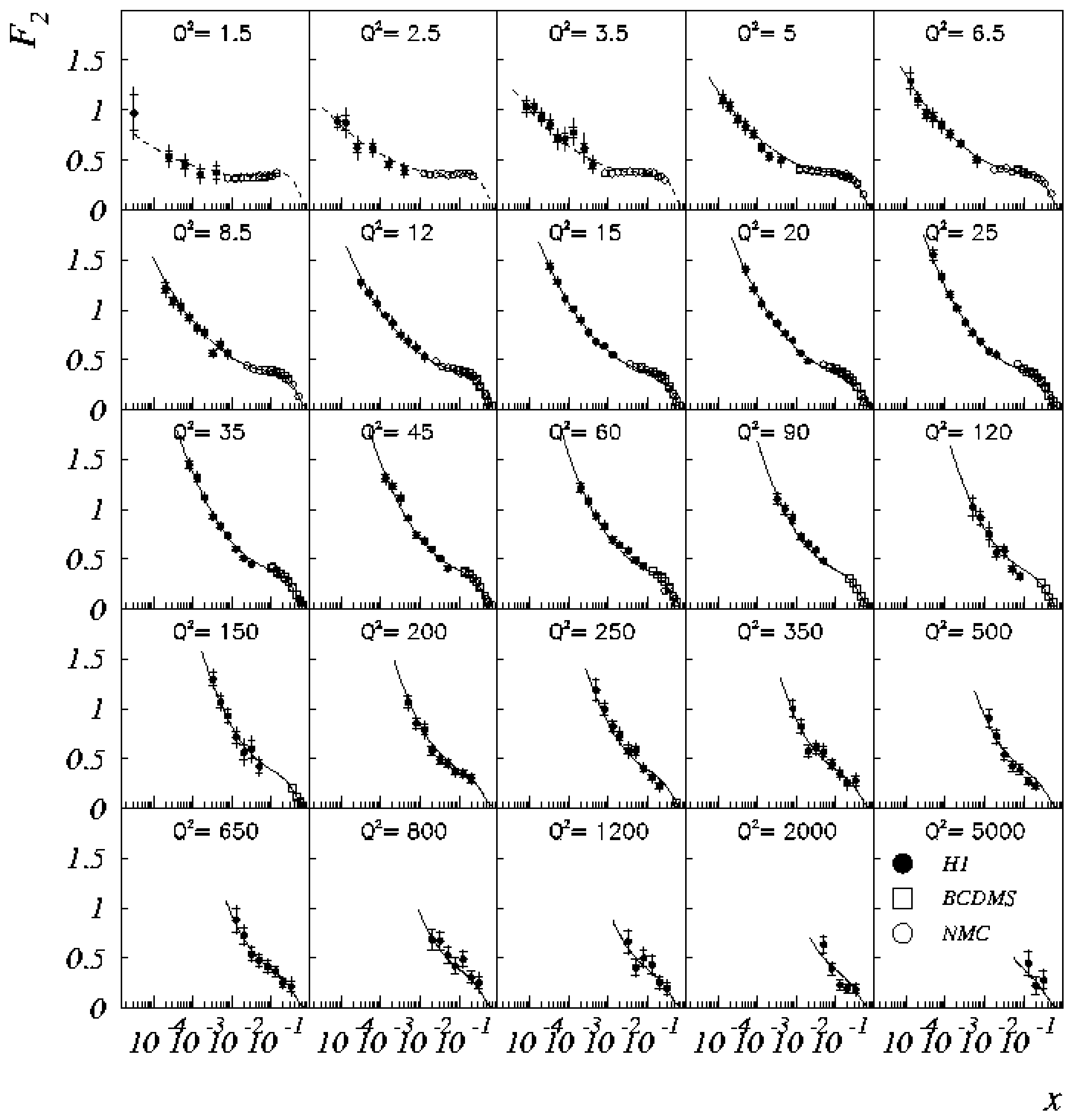

Figure 7: *Measurement of the structure function $F_2(x, Q^2)$ as a function of x. The closed circles are the results of this analysis, the open circles are results taken from the recent publication of the NMC [40] and the open squares results from BCDMS [41]. The inner error bar is the statistical error. The full error bar represents the statistical and systematic errors added in quadrature and disregarding the luminosity error. Additionally a data point has also been measured at $Q^2 = 2$ GeV^2 (see Table 7, not shown in the Figure). The curves represent the NLO QCD fit described in section 7.4, which includes the data for $Q^2 \geq 5$ GeV^2. The extension of the curves below 5 GeV^2 represents only the backward evolution of the fit.*

7 Discussion of the Results

7.1 Phenomenological Fits to the Data

The x and Q^2 behaviour of F_2 can be described by a phenomenological ansatz of the type

$$F_2(x, Q^2) = [a \cdot x^b + c \cdot x^d \cdot (1 + e \cdot \sqrt{x}) \cdot (\log Q^2 + f \log^2 Q^2 + h/Q^2)] \cdot (1 - x)^g, \qquad (8)$$

where Q^2 is given in GeV^2. This functional form was introduced in detail previously [4]. An extra $1/Q^2$ term has been added in order to get a good description at Q^2 below 5 GeV^2. Note that this term is not a measure of higher twist contributions. For the fit, results from

a	b	c	d	e	f	g	h
3.10	0.76	0.124	-0.188	-2.91	-0.043	3.69	1.40

Table 3: *Parameters of a phenomenological fit to the proton structure function results from this experiment combined with F_2 measurements from the NMC and the BCDMS experiments. The parametrization is valid for 1.5 GeV^2 $< Q^2 <$ 5000 GeV^2, $3{\cdot}10^{-5} < x < 1$ and $Q^2 < x{\cdot}10^5$ GeV^2. The parameter h is given in GeV^2.*

H1, NMC [40] and BCDMS [41] are used and statistical and systematic errors were added in quadrature. The parameter values quoted in Table 3 are close to those obtained with 1993 data. The fit provides a good description of all data from the experiments with a χ^2/dof of 1.65 using full errors. For the H1 data alone the parametrization gives a χ^2/dof of 1.00.

In perturbative QCD the rate of growth of F_2 towards low x is expected to increase with increasing Q^2 [6]. The wide range of momentum transfer covered in this experiment enables a study of the Q^2 dependence of the power λ characterizing the rise of $F_2 \propto x^{-\lambda}$ at low x. For each Q^2 bin and $x < 0.1$ the exponent λ was determined taking into account the point-to-point systematic error correlations. The result is given in Table 4 and displayed in Fig. 8. A rise of λ with $\log Q^2$ is observed in the covered range from about 0.2 to 0.4 between 1.5 and 800 GeV^2.

The structure function F_2 is related to the total cross-section of the virtual photon-proton interaction, $\sigma_{tot}(\gamma^* p)$, via

$$\sigma_{tot}(\gamma^* p) \simeq \frac{4\,\pi^2 \alpha}{Q^2} F_2(W, Q^2). \qquad (9)$$

At low x, W is equal to $\sqrt{Q^2/x}$. The λ parameter thus also determines the dependence of F_2 on the invariant mass squared W^2 of the virtual photon-proton ($\gamma^* p$) system. For hadronic and real photoproduction total cross sections the value of λ has been measured to be around 0.08 [42], which is interpreted as the intercept of the so called soft pomeron. For virtual photon-proton interactions λ is found to be substantially larger, and increases with Q^2. Future analyses of HERA data, which will lead to F_2 measurements at Q^2 below 1 GeV^2, should allow the transition between deep-inelastic scattering and real photoproduction to be studied.

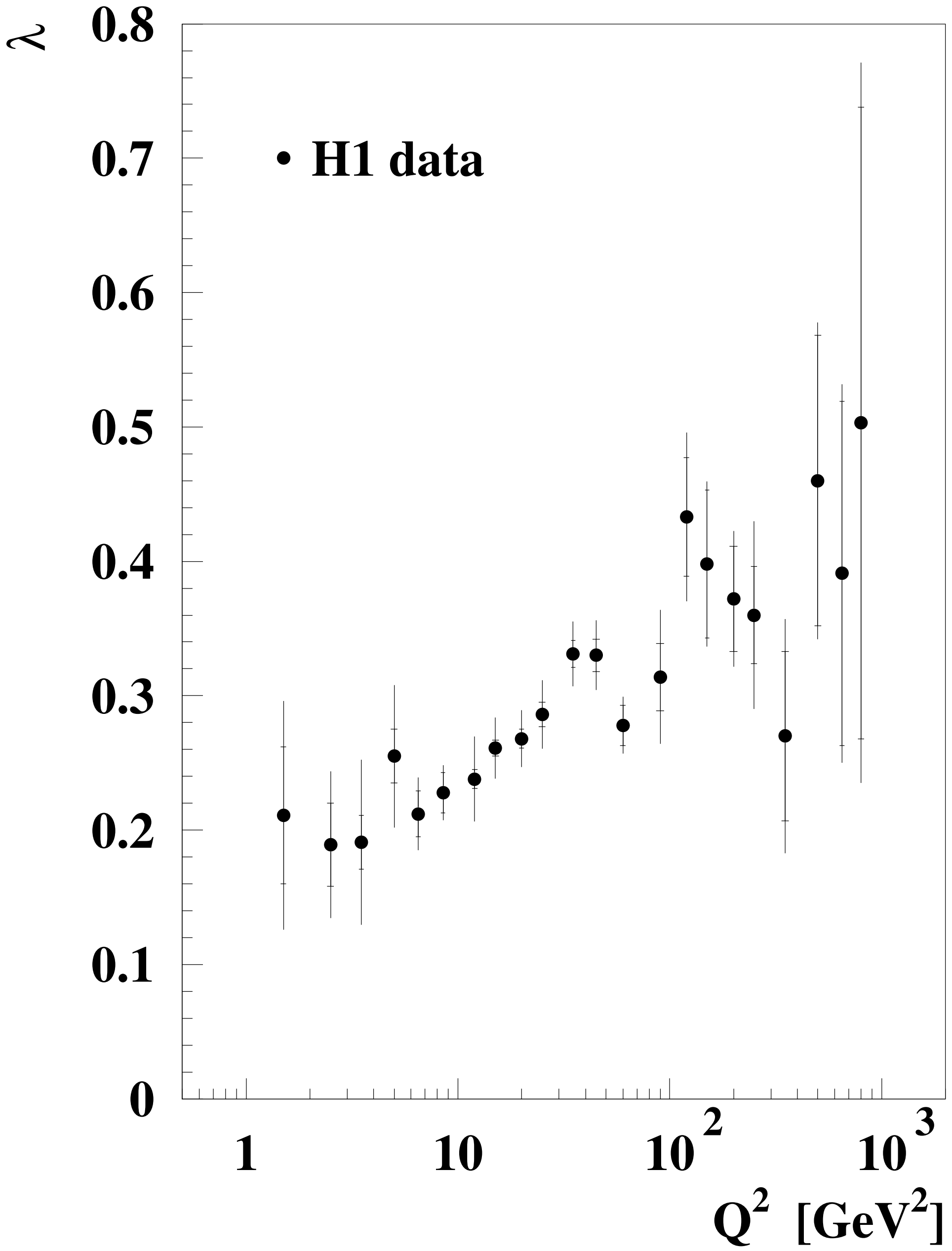

Figure 8: *Variation of the exponent λ from fits of the form $F_2 \sim x^{-\lambda}$ at fixed Q^2 values and $x < 0.1$.*

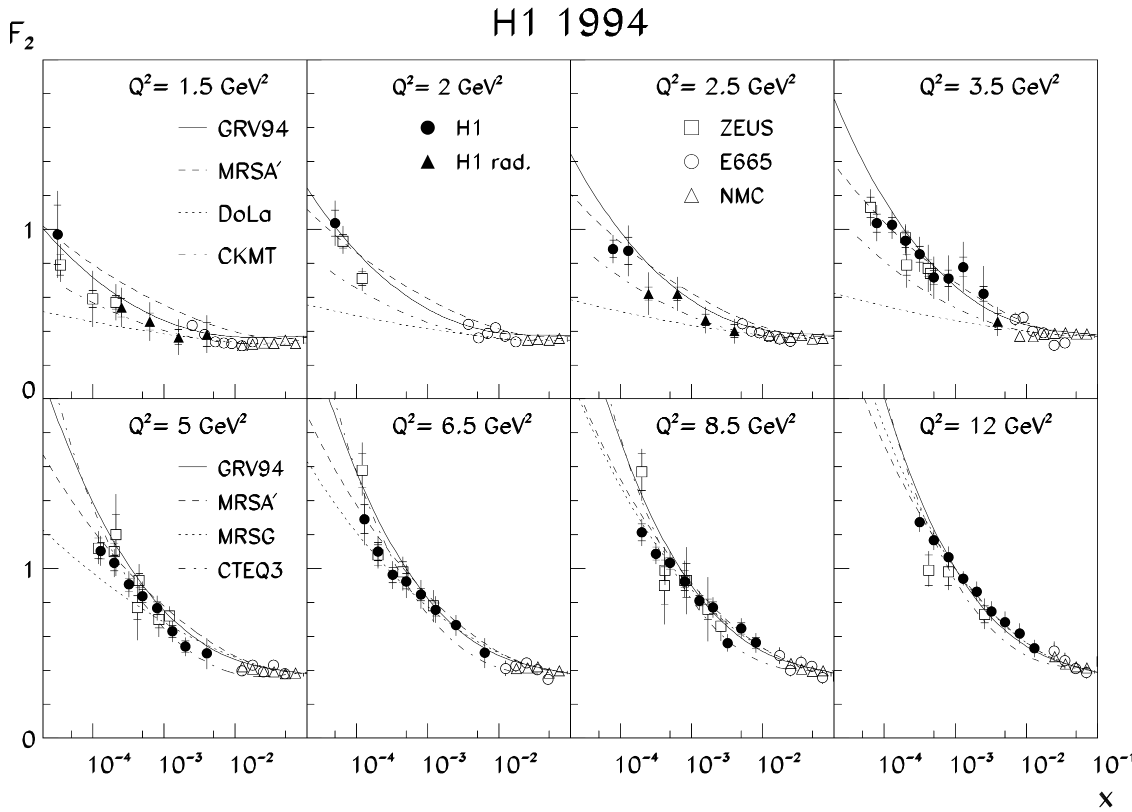

Figure 9: *Measurement of the proton structure function $F_2(x, Q^2)$ in the low Q^2 region by H1 (closed circles: non-radiative events; closed triangles: radiative events), together with results from the ZEUS [36] (open squares), E665 [43] (open circles) and NMC [40] (open triangles) experiments. The Q^2 values of the ZEUS data shown for the bins Q^2 =3.5, 5 and 6.5 GeV^2 are measurements at 3.0, 4.5 and 6 GeV respectively. Different parametrizations for F_2 are compared to the data. The DOLA and CKMT curves are only shown for the upper row of Q^2 bins; CTEQ3M and MRSG are shown for the lower row; GRV and MRSA$'$ are shown for the full Q^2 range.*

Q^2/GeV^2	λ	$\delta\lambda_{stat}$	$\delta\lambda_{syst}$	Q^2/GeV^2	λ	$\delta\lambda_{stat}$	$\delta\lambda_{syst}$
1.5	0.211	0.051	0.068	45	0.330	0.012	0.023
2.5	0.189	0.031	0.045	60	0.278	0.015	0.015
3.5	0.191	0.020	0.058	90	0.314	0.025	0.043
5.0	0.255	0.020	0.049	120	0.433	0.044	0.045
6.5	0.212	0.017	0.021	150	0.398	0.055	0.027
8.5	0.228	0.015	0.014	200	0.372	0.039	0.032
12	0.238	0.007	0.031	250	0.360	0.036	0.060
15	0.261	0.006	0.022	350	0.270	0.063	0.060
20	0.268	0.007	0.020	500	0.460	0.108	0.047
25	0.286	0.009	0.024	650	0.391	0.128	0.059
35	0.331	0.010	0.022	800	0.503	0.235	0.129

Table 4: *The values of the exponent λ as a function of Q^2.*

7.2 Comparison with Models at Low Q^2

Figures 7 and 9 clearly demonstrate the rise of F_2 with decreasing x. In Fig. 9 the data from the eight lowest Q^2 bins are shown[2] and compared with recent data and F_2 parametrizations. The rise of F_2 towards low x is also present in the low Q^2 region. The measurement is in good agreement with the data from the ZEUS experiment [36] and matches well with the data from fixed target experiments [43, 40] at higher x values.

The curves denoted as MRSA′, MRSG [44], CTEQ3M [45] and GRV [19] are parametrizations based on the conventional QCD evolution equations. These calculations assume a certain shape of the x behaviour at a starting Q_0^2 value and use the DGLAP [7] equations to get predictions at different Q^2 values. The MRS and CTEQ distributions assume an $x^{-\lambda}$ behaviour for $x \to 0$ at starting Q_0^2 of a few GeV^2. Their parameters were determined using also the 1993 HERA structure function data.

The GRV calculation assumes that all parton distributions at very low $Q_0^2 = 0.34$ GeV^2 have a valence like shape, i.e. vanish for $x \to 0$. Assuming that the DGLAP equations can be used to evolve the parton distributions from this low Q_0^2 scale to larger Q^2 values, they predicted that the structure function F_2 should rise towards low x even for low values of $Q^2 \sim 1$ GeV^2 [19]. The determination of the shape parameters of the distributions at the starting scale uses only data from fixed target experiments and not much freedom is left for further adjustments in the kinematic range of the HERA data. Small variations are connected with changes still possible in the starting Q_0^2 and the value of the QCD parameter Λ. Fig. 9 shows that the GRV distributions describe the data well, indicating that in this kinematic regime the sea quark distributions can be produced by QCD dynamics.

Parametrizations motivated by Regge theory relate the structure function to Reggeon exchange phenomena which successfully describe the slow rise of the total cross section with

[2] For the radiative data points (triangles in Fig. 9) the y variable cannot be calculated using Q^2/sx with the nominal s since each bin has a different mean incoming electron energy. The average y values are 0.143, 0.063, 0.026, 0.010 for $Q^2 = 1.5$ GeV^2 and 0.199, 0.086, 0.036, 0.015 for $Q^2 = 2.5$ GeV^2, starting at the smallest given x value. For the single point at $Q^2 = 3.5$ GeV^2 $y = 0.018$.

the centre of mass system energy in hadron-hadron and γp interactions. Using the "bare" instead of the "effective" pomeron intercept, the CKMT [46] parametrization rises faster with x compared to former DOLA [47] calculations. The CKMT curves were calculated using the parameters as given in [46], without QCD evolution in the whole range.

The predictions for the Regge inspired models DOLA and CKMT lie below the data for $Q^2 \geq 2$ GeV at low x. The latter were already shown to be significantly below the H1 data of 1993 [48]. The GRV and MRSA′ parametrizations give a good description of the data in the range shown, with the possible exception of the first Q^2 bin for the latter. The MRSG and CTEQ3 distributions, which are not available for the lowest Q^2 values, describe the higher Q^2 data well.

7.3 Double Asymptotic Scaling

The success of the GRV approach suggests that the observed rise of the structure function F_2 towards low x is generated by QCD dynamics. This was already observed in 1974 [6] from a study of the behaviour of F_2 in the limit of large Q^2 and low x. In this asymptotic region the QCD evolution determines the shape of F_2. Recently Ball and Forte [49] developed a convenient way to test the asymptotic behaviour of F_2 using two variables

$$\sigma \equiv \sqrt{\log(x_0/x) \cdot \log(\alpha_s(Q_0)/\alpha_s(Q))}, \quad \rho \equiv \sqrt{\frac{\log(x_0/x)}{\log(\alpha_s(Q_0)/\alpha_s(Q))}} \tag{10}$$

where $\alpha_s(Q)$ is evaluated at the two loop level [50].

The parameters x_0 and Q_0^2 have to be determined experimentally. The parameter Q_0^2 is optimized by minimizing the χ^2 of a linear fit of $\log(R'_F F_2)$ versus σ (see below) using data with $Q^2 \geq 5$ GeV^2. This leads to a value of $Q_0^2 = 2.5$ GeV^2. The same procedure was followed for x_0, which showed less sensitivity. The value $x_0 = 0.1$, as suggested in [49, 51], was found to be a good choice. To visualize the double scaling, it was proposed to rescale F_2 with factors R'_F and R_F defined as

$$R_F(\sigma,\rho) = 8.1 \ \exp\left(-2\gamma\sigma + \omega\frac{\sigma}{\rho} + \frac{1}{2}\log(\gamma\sigma) + \log(\frac{\rho}{\gamma})\right)/\xi_F \tag{11}$$

with

$$\xi_F = 1 + ((\xi_1 + \xi_2) * \alpha_s(Q) - \xi_1 * \alpha_s(Q_0)) * (\rho/(2\pi * \gamma)) \tag{12}$$

and

$$R'_F(\sigma,\rho) = R_F \exp(2\gamma\sigma). \tag{13}$$

Here $\xi_1 = (206n_f/27 + 6b_1/b_0)/b_0$, $\xi_2 = 13$, $b_0 = 11 - 2n_f/3$, $\omega = (11 + 2n_f/27)/b_0$ and $b_1 = 102 - 38n_f/3$. The number of flavours is n_f and $\gamma = \sqrt{(12/b_0)}$. The function $\log(R'_F F_2)$ is then predicted to rise linearly with σ. $R_F F_2$ is expected to be independent of ρ and σ. Note that these expectations are valid only if the gluon distribution, which drives F_2 at low x via the sea quarks, does not have a too singular behaviour for $Q^2 = Q_0^2$.

Fig. 10a shows $R_F F_2$ versus ρ for the data with $Q^2 \geq 3.5$ GeV^2. The value of Λ for four flavours was chosen to be 263 MeV [52]. The continuity of $\alpha_s(Q)$ at the bottom quark mass threshold is imposed using the prescription in [38]. Approximate scaling is observed for $Q^2 \geq 5$ GeV^2 and $\rho \geq 2$. At high ρ the low Q^2 data tend to violate the scaling behaviour

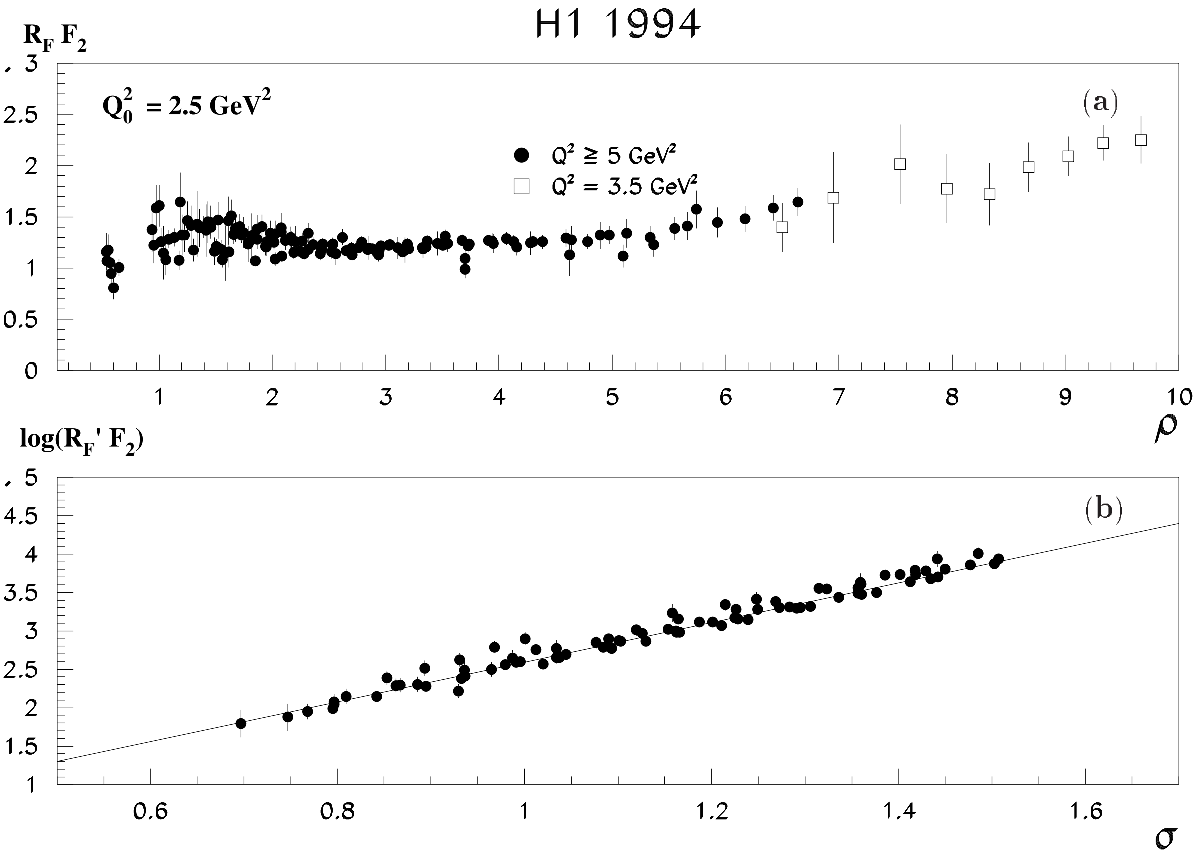

Figure 10: *The rescaled structure functions* **a)** $R_F F_2$ *versus* ρ *and* **b)** $\log(R'_F F_2)$ *versus* σ *(see text). Only data with* $Q^2 \geq 5$ *GeV*^{2} *and* $\rho > 2$ *are shown in b).*

which is seen clearly for the data at 3.5 GeV^2. In Fig. 10b, the results are shown for $\rho \geq 2$ and $Q^2 \geq 5$ GeV^2 as a function of σ. The data exhibit the expected linear rise of $\log(R'_F F_2)$ with σ. A linear fit to the data gives a value for the slope of: 2.50$\pm$0.02$\pm$0.06 (2.57$\pm$0.05$\pm$0.06) for $Q^2 < 15$ GeV^2 ($Q^2 > 35$ GeV^2) and 4 (5) flavours. The first error is the statistical error and the second error is the systematic error taking into account the point-to-point correlations. The value expected from QCD is 2.4 (2.5) for 4 (5) flavours. The results are in agreement with these predictions. Compared to the result presented in [51], the extraction based on the 2-loop formalism used here is in better agreement with QCD expectation. Not included in this error is the influence of the uncertainty in the choice of Λ. Varying Λ by $\pm$65MeV changes the result on the slope by $\mp$0.03.

One can conclude that the low x, low Q^2 measurements for $Q^2 \geq 5$ GeV^2 show scaling in ρ and σ. Thus double asymptotic scaling is a dominant feature of F_2 in this region.

7.4 Extraction of the Gluon Density

In a QCD analysis the evolution equations were solved numerically in the NLO order approximation following the procedure described in [53]. The splitting functions and the strong coupling constant $\alpha_s(Q^2)$ are defined in the $\overline{MS}$ factorization and renormalization schemes. In the DGLAP evolution equations only three light quark flavours are taken into account. Heavy quark contributions are dynamically generated using the photon-gluon fusion (PGF) prescription given in [54, 55], extended to NLO according to [56]. The scale of the PGF process has been taken as $\sqrt{Q^2 + 4m_c^2}$ with a charm quark mass of $m_c = 1.5$ GeV. An uncertainty of the charm quark mass of 0.5 GeV was considered which leads to a few percent variation of the gluon density. The small contribution of beauty quarks has been neglected.

The gluon g, the valence quark u_v and d_v and the non-strange sea S ($S \equiv \bar{u} + \bar{d}$) distributions are parametrized at $Q_0^2 = 5$ GeV^2 in the following way:

$$\begin{aligned}
xg(x) &= A_g x^{B_g}(1-x)^{C_g}, \\
xu_v(x) &= A_u x^{B_u}(1-x)^{C_u}(1 + D_u x + E_u\sqrt{x}), \\
xd_v(x) &= A_d x^{B_d}(1-x)^{C_d}(1 + D_d x + E_d\sqrt{x}), \\
xS(x) &= A_S x^{B_S}(1-x)^{C_S}(1 + D_S x + E_S\sqrt{x}).
\end{aligned} \tag{14}$$

The quark and antiquark components of the sea are assumed to be equal, and $\bar{u}$ is set equal to $\bar{d}$. As determined in [57], the strange quark density is taken to be $S/4$. With these definitions the proton structure function F_2, for $n_f = 3$ and to leading order, is given as

$$F_2(x, Q^2) = \frac{11}{18}xS + \frac{4}{9}xu_v + \frac{1}{9}xd_v. \tag{15}$$

The normalizations of the valence quark densities are fixed using the counting rules $\int_0^1 u_v(x)dx = 2$ and $\int_0^1 d_v(x)dx = 1$. The normalization A_g of the gluon density is obtained via the momentum sum rule. Since no isoscalar data are available yet in the small x domain, $B_u = B_d$ is assumed. The parameters B_S and B_g which govern the small x behaviour of F_2 and of the gluon are allowed to be different. For Λ the value of 263 MeV is taken, as determined in [52].

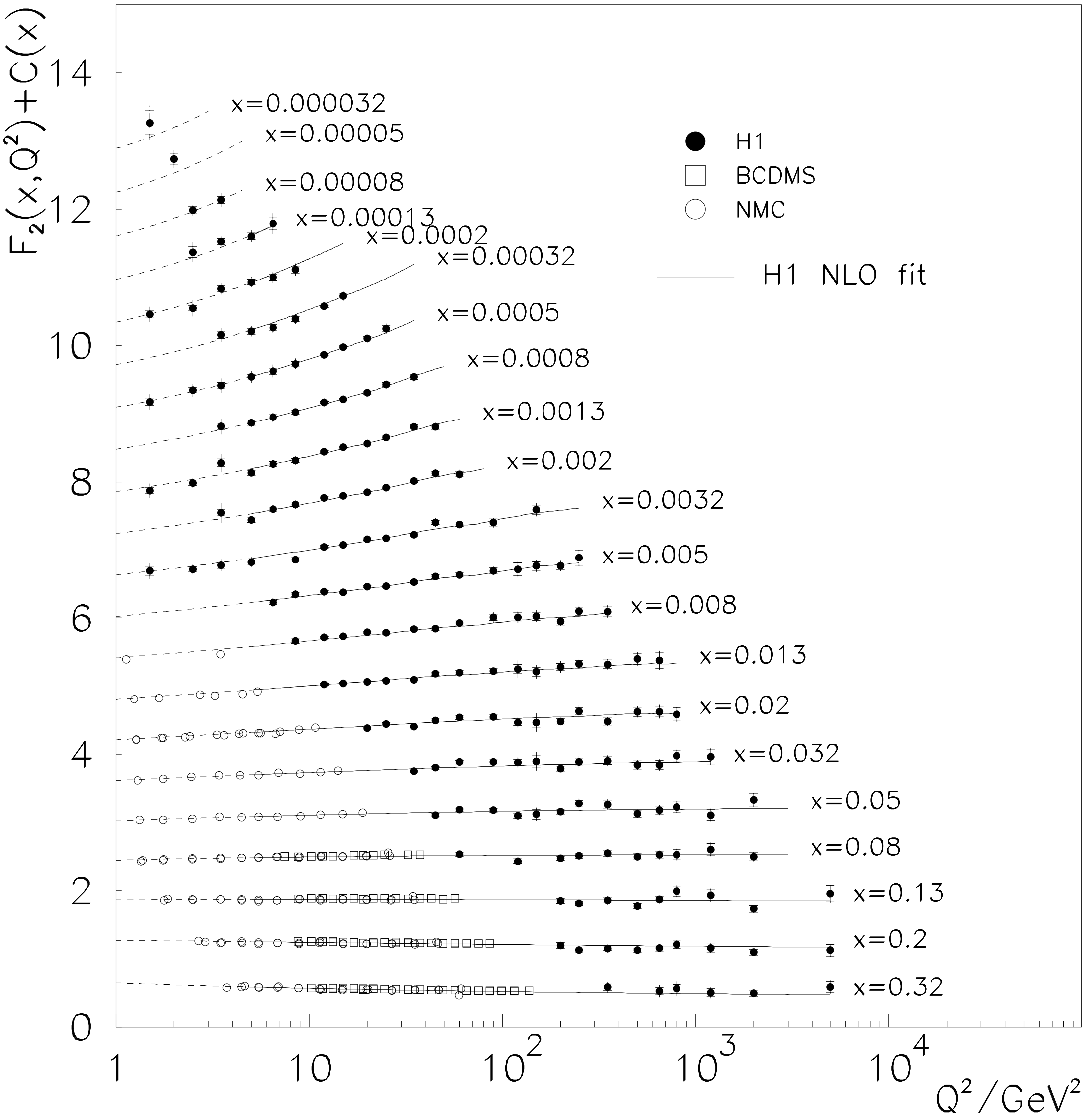

Figure 11: $F_2(x, Q^2)$ *measured by H1 together with BCDMS [41] and NMC [40] fixed target results. The full line corresponds to the NLO QCD fit, see sect.7.4, which includes the data for* $Q^2 \geq 5$ GeV^2. *The extension of the curves below 5* GeV^2 *represents only the backward evolution of the fit. The* F_2 *values are plotted in a linear scale adding a constant* $c(x)= 0.6(i-0.4)$ *where* i *is the* x *bin number starting at* $i=1$ *from* $x = 0.32$. *The inner error bar is the statistical error, the outer corresponds to the full error resulting from adding the statistical and systematic error in quadrature. Some H1 data points at lower* Q^2 *where shifted to nearby* x *values for graphical representation of the data.*

Experiment	H1 nvtx	H1 svtx	NMC-p	NMC-D	BCDMS-p	BCDMS-D	total
data points	157	16	96	96	174	159	698
χ^2 (unco. err.)	174	13	157	153	222	208	931
χ^2 (full error)	85	6	120	114	122	140	591
normalization	1.00	1.04	1.00	1.00	0.97	0.97	

Table 5: *For each experiment are given: the number of data points used in the QCD fit, the χ^2 obtained as described in the text using only the uncorrelated errors, the χ^2 computed from the same fit using the full error on each point and the normalization factors as determined from the fit. The H1 nominal vertex and shifted vertex data samples are denoted as nvtx and svtx respectively.*

In order to constrain the valence quark densities at high x, proton and deuteron results from the BCDMS and NMC experiments are also used. To avoid possible higher twist effects, data in the ranges $Q^2 < 5$ GeV^2, and $Q^2 < 15$ GeV^2 for $x > 0.5$ are not included in the fit. The small contribution of large rapidity gap events in the HERA data is considered to be part of the structure function, as there is no evidence that the QCD evolution of the diffractive part of F_2 is significantly different from that of the total inclusive F_2.

The parton densities are derived from a fit of the evolution equations to the data using the program MINUIT. For the calculation of the χ^2 which was minimized, the statistical errors were combined in quadrature with those systematic errors which are uncorrelated. For BCDMS only statistical errors were included. In addition a term was added to the χ^2 to permit variation of the relative normalization of the different data sets. The following normalization errors were taken into account: H1 (nominal vertex sample): 1.5%, H1 (shifted vertex sample): 3.9%, BCDMS: 3%, and NMC: 2.5%. The χ^2 obtained in this procedure and the χ^2 computed when considering the full error of each point are given in Table 5.

The result of the fit is shown in Fig. 7 versus x and Fig. 11 versus Q^2. The fit gives a good description of all data used. Only small adjustments of the relative normalizations (given in Table 5) are required demonstrating remarkable agreement between these different experiments. In Fig. 7 the steep x behaviour of F_2 is seen to be described very well by the fit. Note that the data for $Q^2 < 5$ GeV^2, which were excluded from the fit, are still well reproduced by the fit evolved backwards in Q^2. However, a definite test of perturbative QCD in this region requires more accurate data and a study of possible higher twist effects, which is beyond the scope of this analysis. The Q^2 dependence at fixed x is also described well over the nearly 4 orders of magnitude in Q^2 covered by the H1 data, see Fig. 11. The parameters of the initial distributions are listed in Table 6. There are sizeable correlations between these parameters which were not studied in detail as the basic aim of this analysis was to extract the gluon density.

Fig. 12 shows the NLO gluon density $xg(x, Q^2)$ at $Q^2 = 5$ GeV^2 and $Q^2 = 20$ GeV^2. Note that there are no F_2 measurements below $5 \cdot 10^{-4}$ at $Q^2 = 20$ GeV^2, but in that region the gluon is constrained by the data at lower Q^2 via the QCD evolution equations. The experimental error band was determined in two steps: the initial error was obtained directly from the fit when considering only the uncorrelated errors of the data points which are dominated by the statistical errors of the F_2 measurement. Then the systematic errors

A_g	B_g	C_g			A_u	B_u	C_u	D_u	E_u
2.24	−0.20	8.52			2.84	0.55	4.19	4.42	−1.40
A_S	B_S	C_S	D_S	E_S	A_d	B_d	C_d	D_d	E_d
0.27	−0.19	1.66	0.16	−1.00	1.05	0.55	6.44	−1.16	3.87

Table 6: *The values of the parameters at Q^2 =5 GeV^2 of the gluon, the sea quark and valence quark densities, as determined from the QCD fit.*

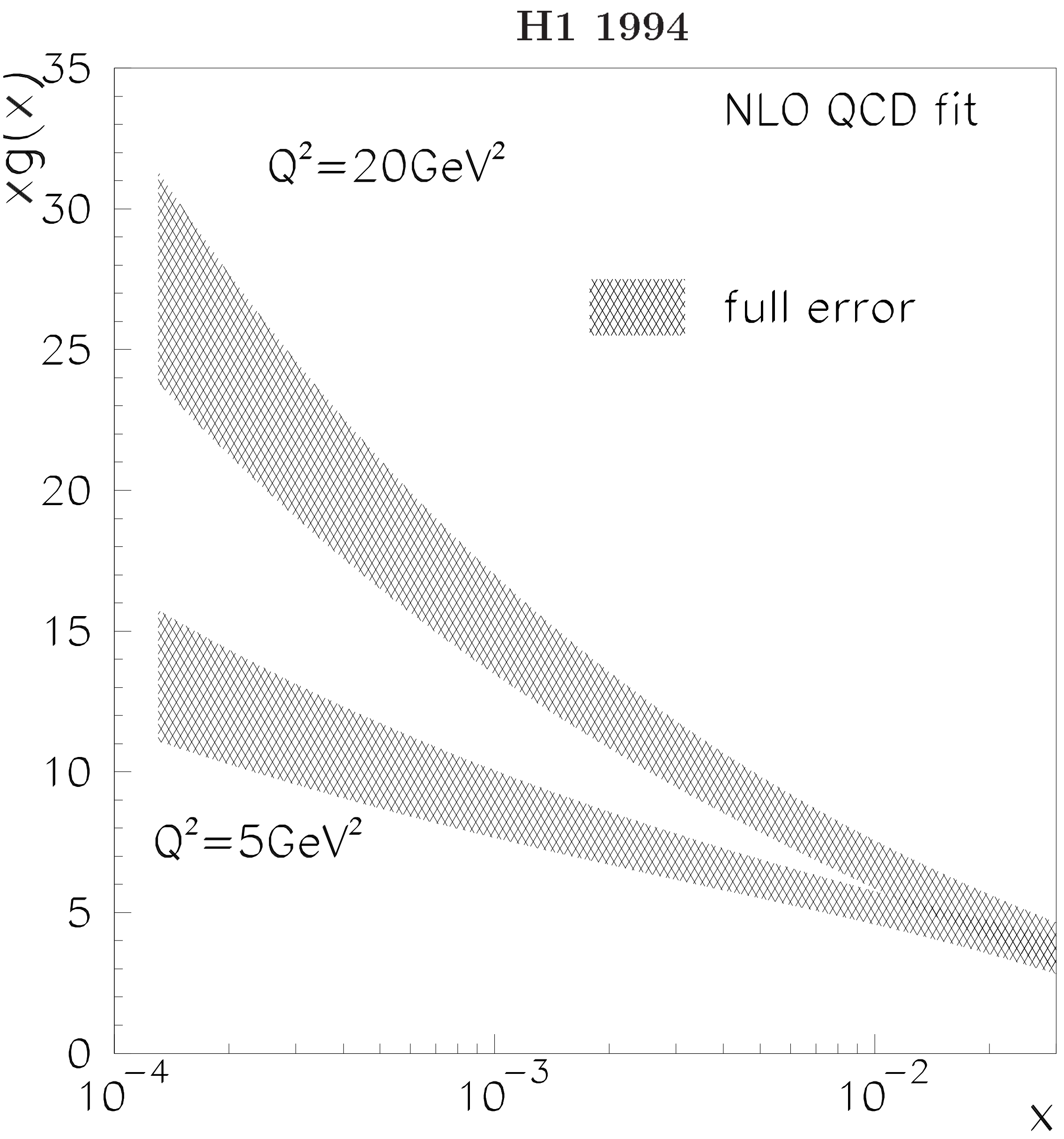

Figure 12: *The gluon density $xg(x)$ at Q^2 = 5 GeV^2 and Q^2 = 20 GeV^2 extracted from a NLO QCD fit. The procedure to derive the error bands is explained in the text.*

introducing point-to-point correlations, as for instance a possible shift in the scattered electron energy, were treated in a procedure described in [51]. Their effect was added quadratically to the effect from the uncorrelated ones, determining the full experimental error band of the measurement of xg. A variation of Λ by 65 MeV [52] gives a change of 9% on the gluon density at 20 GeV^2 which has not been added to the errors shown in Fig. 12.

The accuracy of this determination of xg is better by about a factor of two than the H1 result based on the 1993 data [51]. A rise of the gluon density towards low x is observed which is related to the behaviour of $F_2 \propto x^{-\lambda}$. Accordingly, the rise of xg towards low x increases with increasing Q^2.

8 Summary

A measurement has been presented of the proton structure function $F_2(x, Q^2)$ in deep-inelastic electron-proton scattering at HERA with data taken in the running period of 1994. The integrated luminosity is 2.7 pb^{-1} which represents a tenfold increase in statistics compared to the F_2 analysis based on the 1993 data of the H1 experiment. The structure function measurement includes data from different detector components and running configurations. Low Q^2 values are reached using data with the ep interaction vertex shifted from the nominal position and with radiative events. The data cover a kinematic range for Q^2 between 1.5 and 5000 GeV^2 and x between $3.0 \cdot 10^{-5}$ and 0.32.

The F_2 values presented are obtained using different methods to reconstruct the inclusive scattering kinematics. At high values of the scaling variable $y \geq 0.15$, due to its superior resolution, the method used is based on the scattered electron energy and angle. Lower y values are covered with a method which combines electron and hadronic information to reduce radiative corrections and calibration errors. A smooth transition is observed from the fixed target high x data to the HERA low x data.

The rise of the structure function with decreasing x at fixed Q^2 is confirmed. The rate of growth increases with increasing Q^2 which has been one of the very first predictions of perturbative QCD. Approximate scaling in double logarithmic variables depending on x and Q^2 is observed using a recent 2 loop QCD calculation. The data are well described in the full x and Q^2 range by a NLO fit based on the conventional DGLAP evolution equations. The fit results are used to measure the gluon distribution with improved precision down to $x = 10^{-4}$. The gluon density rises significantly for decreasing values of x.

Acknowledgements

We are very grateful to the HERA machine group whose outstanding efforts made this experiment possible. We acknowledge the support of the DESY technical staff. We appreciate the big effort of the engineers and technicians who constructed and maintain the detector. We thank the funding agencies for financial support of this experiment. We wish to thank the DESY directorate for the support and hospitality extended to the non-DESY members of the collaboration. Finally, helpful discussions are acknowledged with R. Ball, D. Bardin, J. Blümlein, R.Peschanski, H. Spiesberger and A. Vogt.

References

[1] for recent reviews see: F. Eisele, Proceedings of the 1995 International Europhysics Conference on High Energy Physics, Brussels, DESY-95-229;
A. Caldwell, Proceedings of the 1995 International Symposium on Lepton and Photon Interactions at High Energies, Beijing, DESY-95-231.

[2] H1 Collaboration, I. Abt et al., Nucl. Phys. **B407** (1993) 515.

[3] ZEUS Collaboration, M. Derrick et al., Phys. Lett. **B316** (1993) 412.

[4] H1 Collaboration, T. Ahmed et al., Nucl. Phys. **B439** (1995) 471.

[5] ZEUS Collaboration, M. Derrick et al., Z. Phys. **C65** (1995) 379.

[6] A. De Rújula et al., Phys. Rev. **D10** (1974) 1649.

[7] Yu. L. Dokshitzer, Sov. Phys. JETP **46** (1977) 641;
V. N. Gribov and L.N. Lipatov, Sov. J. Nucl. Phys. **15** (1972) 438 and 675;
G. Altarelli and G. Parisi, Nucl. Phys. **B126** (1977) 298.

[8] E. A. Kuraev, L. N. Lipatov and V. S. Fadin, Sov. Phys. JETP **45** (1977) 199;
Y. Y. Balitsky and L.N. Lipatov, Sov. J. Nucl. Phys. **28** (1978) 822.

[9] L. V. Gribov, E. M. Levin and M. G. Ryskin, Phys. Rep. **100** (1983) 1;
A. H. Mueller and J. Qiu, Nucl. Phys. **B268** (1986) 427.

[10] H1 Collaboration, S. Aid et al., Phys. Lett. **B356** (1995) 118.

[11] U. Bassler and G. Bernardi, Nucl. Instr. and Meth. **A361** (1995) 197.

[12] H1 Collaboration, I. Abt et al., DESY 93-103 (1993).

[13] H1 BEMC Group, J. Bán et al., DESY 95-177 (1995), to appear in Nucl. Instr. and Meth. **A**.

[14] H1 Calorimeter Group, B. Andrieu et al., Nucl. Instr. and Meth. **A336** (1993) 460.

[15] H1 Collaboration, T. Ahmed et al., Z. Phys. **C66** (1995) 529.

[16] G. A. Schuler and H. Spiesberger, Proceedings of the Workshop Physics at HERA, vol. 3, eds. W. Buchmüller, G. Ingelman, DESY (1992) 1419.

[17] A. Kwiatkowski, H. Spiesberger and H.-J. Möhring, Computer Phys. Comm. **69** (1992) 155.

[18] G. Ingelman, Proceedings of the Workshop Physics at HERA, vol. 3, eds. W. Buchmüller, G. Ingelman, DESY (1992) 1366.

[19] M. Glück, E. Reya and A. Vogt, Z. Phys **C67** (1995) 433;
We show the parametrizations as presented in:
A. Vogt, Proceedings of the Workshop on Deep-Inelastic Scattering and QCD, Paris (1995) 261,
using the NLO charm contribution as calculated in [56].

[20] L. Lönnblad, Comp. Phys. Comm. **71** (1992) 15.

[21] H1 Collaboration, I. Abt et al., Z. Phys. **C63** (1994) 377.

[22] ZEUS Collaboration, M. Derrick et al., Z. Phys. **C59** (1993) 231.

[23] G. Marchesini et al., Comp. Phys. Comm. **67** (1992) 465.

[24] R. Engel, Proceedings of the XXIXth Rencontre de Moriond, ed. J. Tran Thanh Van, (edition frontieres, 1994) 321.

[25] H. U. Bengtsson and T. Sjöstrand, Computer Phys. Comm. **46** (1987) 43.

[26] N. H. Brook, A. De Roeck and A. T. Doyle, RAYPHOTON 2.0, Proceedings of the Workshop Physics at HERA, vol. 3, eds. W. Buchmüller, G. Ingelman, DESY (1992) 1453.

[27] ZEUS Collaboration, M. Derrick et al., Phys. Lett. **B315** (1993) 481,
H1 Collaboration, T.Ahmed et al., Nucl. Phys. **B429** (1994) 477.

[28] H. Jung, Comp. Phys. Comm. **86** (1995) 147.

[29] R. Brun et al., GEANT3 User's Guide, CERN–DD/EE 84–1, Geneva (1987).

[30] A. Panitch, Ph.D. Thesis, University of Brussels (1996), in litt.

[31] C. Hoeger, Proceedings of the Workshop Physics at HERA, vol. 1, eds. W. Buchmüller, G. Ingelman, DESY (1992) 43.
S. Bentvelsen et al., Proceedings of the Workshop Physics at HERA, vol. 1, eds. W. Buchmüller, G. Ingelman, DESY (1992) 23.

[32] B. Gonzalez-Pineiro, Ph.D. Thesis, University of Paris (1996), in litt.

[33] J. Lipinski, Ph.D. Thesis, University of Hamburg (1996), in litt.

[34] L. Favart, Ph.D. Thesis, University of Brussels (1995).

[35] L. Favart et al., DESY grey report 96/01 (1996).

[36] ZEUS Collaboration, M. Derrick et al., DESY preprint 95-193 (1995).

[37] G. Altarelli and G. Martinelli, Phys. Lett. **B76** (1978) 89.

[38] W.J. Marciano, Phys. Rev. **D29** (1984) 580.

[39] A. Arbuzov et al., DESY preprint 95-185 (1995).

[40] NMC Collaboration, M. Arneodo et al., Phys. Lett. **B364** (1995) 107.

[41] BCDMS Collaboration, A.C. Benvenuti et al., Phys. Lett. **B223** (1989) 485;
CERN preprint CERN-EP/89-06.

[42] A. Donnachie and P. V. Landshoff, Phys. Lett. **B296** (1992) 227.

[43] E665 Collaboration, M.R. Adams et al., FNAL-Pub-95/396-E (1995).

[44] A.D. Martin, W.J. Stirling and R.G. Roberts, Phys. Lett. **B354** (1995) 155.

[45] CTEQ Collaboration, J. Botts et al. , Phys. Lett. **B304** (1993) 15;
CTEQ Collaboration, J. Botts et al. (to be published).

[46] A. Capella et al., Phys. Lett. **B337** (1994) 358.

[47] A. Donnachie and P. V. Landshoff, Z. Phys. **C61** (1994) 139.

[48] A. De Roeck, DESY preprint, 95-025 (1995).

[49] R.D. Ball, S. Forte, Phys. Lett. **B335** (1994) 77.

[50] R.D. Ball and S. Forte, "XXXV Cracow School of Theoretical Physics", Zakopane, June 1995, to be published in Acta Phys. Pol.

[51] H1 Collaboration, S. Aid et al., Phys. Lett. **B354** (1995) 494.

[52] M. Virchaux and A. Milsztajn, Phys. Lett. **B274** (1992) 221.

[53] C. Pascaud and F. Zomer, LAL preprint LAL/94-42.

[54] M. Glück, E. Hoffmann and E. Reya, Z. Phys. **C13** (1982) 119.

[55] M. Glück, E. Reya and M. Stratmann, Nucl. Phys. **B422** (1994) 37.

[56] E.Laenen et al., Nucl. Phys. **B392** (1993) 162, 229;
E.Laenen et al., Phys. Lett. **B291** (1992) 325;
S.Riemersma et al., Phys. Lett. **B347** (1995) 143.

[57] CCFR Collaboration, A.O. Bazarko et al., Z. Phys. **C65** (1995) 189.

Q^2	x	F_2	δ_{stat}	δ_{syst}	R
1.5	.00003	0.969	0.176	0.187	0.71
1.5	.00025	0.540	0.055	0.104	0.75
1.5	.00063	0.458	0.050	0.101	0.74
1.5	.00158	0.365	0.045	0.095	0.70
1.5	.00398	0.381	0.070	0.087	0.63
2.0	.00005	1.037	0.077	0.110	0.65
2.5	.00008	0.885	0.052	0.065	0.80
2.5	.00013	0.874	0.079	0.127	0.80
2.5	.00025	0.622	0.037	0.119	0.80
2.5	.00063	0.621	0.039	0.093	0.79
2.5	.00158	0.466	0.033	0.072	0.75
2.5	.00398	0.402	0.039	0.062	0.65
3.5	.00008	1.036	0.053	0.092	0.64
3.5	.00013	1.026	0.045	0.067	0.64
3.5	.00020	0.934	0.041	0.075	0.64
3.5	.00032	0.854	0.046	0.093	0.64
3.5	.00050	0.716	0.041	0.119	0.64
3.5	.00080	0.712	0.049	0.126	0.63
3.5	.00130	0.778	0.058	0.137	0.61
3.5	.00250	0.621	0.043	0.157	0.59
3.5	.00398	0.458	0.046	0.075	0.54
5.0	.00013	1.106	0.049	0.074	0.54
5.0	.00020	1.033	0.044	0.069	0.54
5.0	.00032	0.907	0.039	0.066	0.54
5.0	.00050	0.839	0.039	0.076	0.53
5.0	.00080	0.769	0.037	0.063	0.53
5.0	.00130	0.630	0.034	0.050	0.51
5.0	.00200	0.540	0.033	0.043	0.50
5.0	.00400	0.500	0.029	0.086	0.46
6.5	.00013	1.292	0.085	0.127	0.49
6.5	.00020	1.101	0.052	0.072	0.48
6.5	.00032	0.963	0.045	0.068	0.48
6.5	.00050	0.926	0.044	0.088	0.48
6.5	.00080	0.848	0.038	0.076	0.47
6.5	.00130	0.759	0.039	0.068	0.46
6.5	.00250	0.667	0.029	0.054	0.43
6.5	.00630	0.504	0.029	0.084	0.37
8.5	.00020	1.215	0.050	0.062	0.44
8.5	.00032	1.089	0.038	0.048	0.44
8.5	.00050	1.033	0.034	0.062	0.43
8.5	.00080	0.923	0.031	0.038	0.43
8.5	.00130	0.811	0.030	0.047	0.42
8.5	.00200	0.770	0.034	0.049	0.40
8.5	.00320	0.562	0.028	0.043	0.38
8.5	.00500	0.648	0.033	0.051	0.36
8.5	.00800	0.564	0.032	0.049	0.33
12.	.00032	1.276	0.020	0.055	0.39
12.	.00050	1.168	0.016	0.056	0.39
12.	.00080	1.067	0.015	0.061	0.38
12.	.00130	0.942	0.015	0.039	0.37
12.	.00200	0.866	0.016	0.057	0.36
12.	.00320	0.749	0.016	0.055	0.34
12.	.00500	0.685	0.016	0.061	0.32
12.	.00800	0.618	0.016	0.057	0.30
12.	.01300	0.531	0.017	0.049	0.26
15.	.00032	1.426	0.030	0.064	0.37
15.	.00050	1.280	0.020	0.050	0.36
15.	.00080	1.110	0.018	0.057	0.35
15.	.00130	1.008	0.016	0.033	0.35
15.	.00200	0.895	0.015	0.046	0.34
15.	.00320	0.773	0.014	0.036	0.32
15.	.00500	0.677	0.014	0.035	0.30
15.	.00800	0.634	0.014	0.031	0.28
15.	.01300	0.547	0.013	0.027	0.24
20.	.0005	1.407	0.026	0.054	0.34
20.	.0008	1.210	0.022	0.050	0.33
20.	.0013	1.061	0.020	0.055	0.33
20.	.0020	0.945	0.018	0.042	0.32
20.	.0032	0.861	0.017	0.038	0.31
20.	.0050	0.761	0.017	0.028	0.30
20.	.0080	0.693	0.016	0.035	0.28
20.	.0130	0.567	0.015	0.024	0.26
20.	.0200	0.487	0.015	0.025	0.22
25.	.0005	1.546	0.047	0.058	0.40
25.	.0008	1.330	0.028	0.051	0.39
25.	.0013	1.151	0.024	0.047	0.38
25.	.0020	1.019	0.022	0.035	0.37
25.	.0032	0.872	0.020	0.034	0.35
25.	.0050	0.768	0.019	0.034	0.33
25.	.0080	0.683	0.018	0.031	0.30
25.	.0130	0.585	0.017	0.028	0.26
25.	.0200	0.548	0.017	0.037	0.22
35.	.0008	1.442	0.038	0.051	0.36
35.	.0013	1.308	0.032	0.052	0.35
35.	.0020	1.116	0.027	0.052	0.33
35.	.0032	0.928	0.024	0.038	0.32
35.	.0050	0.832	0.023	0.040	0.30
35.	.0080	0.739	0.022	0.035	0.27
35.	.0130	0.600	0.019	0.025	0.24
35.	.0200	0.508	0.019	0.019	0.20
35	.0320	0.452	0.019	0.026	0.16
45.	.0013	1.305	0.038	0.048	0.32
45.	.0020	1.225	0.034	0.049	0.31
45.	.0032	1.105	0.032	0.058	0.30
45.	.0050	0.912	0.028	0.033	0.28
45.	.0080	0.743	0.025	0.029	0.26
45.	.0130	0.686	0.024	0.031	0.22

Table 7: *Proton structure function $F_2(x,Q^2)$ with statistical and systematic errors, part I. The normalization uncertainty, not included in the systematic error, is 1.5% for $Q^2 > 8.5$*

Q^2	x	F_2	δ_{stat}	δ_{syst}	R
45.	.0200	0.599	0.022	0.027	0.19
45.	.0320	0.505	0.021	0.023	0.15
45.	.0500	0.411	0.022	0.028	0.12
60.	.0020	1.213	0.042	0.048	0.29
60.	.0032	1.079	0.037	0.045	0.28
60.	.0050	0.937	0.033	0.043	0.26
60.	.0080	0.830	0.031	0.046	0.24
60.	.0130	0.701	0.028	0.029	0.21
60.	.0200	0.639	0.027	0.025	0.18
60.	.0320	0.586	0.026	0.028	0.14
60.	.0500	0.492	0.025	0.023	0.11
60.	.0800	0.432	0.027	0.023	0.08
90.	.0032	1.103	0.052	0.048	0.26
90.	.0050	0.997	0.045	0.047	0.24
90.	.0080	0.908	0.041	0.056	0.22
90.	.0130	0.726	0.035	0.040	0.19
90.	.0200	0.650	0.033	0.031	0.17
90.	.0320	0.587	0.030	0.034	0.13
90.	.0500	0.481	0.027	0.019	0.10
120.	.0050	1.018	0.094	0.076	0.23
120.	.0080	0.914	0.068	0.056	0.21
120.	.0130	0.755	0.063	0.111	0.18
120.	.0200	0.570	0.049	0.057	0.16
120.	.0320	0.582	0.048	0.060	0.13
120.	.0500	0.402	0.035	0.045	0.10
120.	.0800	0.330	0.032	0.034	0.07
150.	.0032	1.292	0.069	0.067	0.23
150.	.0050	1.067	0.065	0.057	0.22
150.	.0080	0.928	0.061	0.060	0.20
150.	.0130	0.716	0.064	0.079	0.17
150.	.0200	0.566	0.069	0.114	0.15
150.	.0320	0.598	0.085	0.103	0.12
150.	.0500	0.424	0.071	0.065	0.09
200.	.005	1.065	0.059	0.053	0.21
200.	.008	0.853	0.051	0.038	0.19
200.	.013	0.787	0.052	0.071	0.17
200.	.020	0.585	0.041	0.023	0.14
200.	.032	0.490	0.038	0.026	0.11
200.	.050	0.460	0.039	0.029	0.09
200.	.080	0.372	0.032	0.039	0.06
200.	.130	0.350	0.037	0.032	0.04
200.	.200	0.301	0.045	0.036	0.03
250.	.005	1.185	0.106	0.060	0.20
250.	.008	1.000	0.062	0.054	0.18
250.	.013	0.826	0.055	0.047	0.16
250.	.020	0.730	0.051	0.072	0.14
250.	.032	0.590	0.044	0.067	0.11
250.	.050	0.584	0.043	0.060	0.09

Q^2	x	F_2	δ_{stat}	δ_{syst}	R
250.	.080	0.408	0.033	0.037	0.06
250.	.130	0.312	0.029	0.051	0.04
250.	.200	0.231	0.031	0.056	0.03
350.	.008	0.997	0.082	0.049	0.17
350.	.013	0.825	0.066	0.043	0.15
350.	.020	0.581	0.052	0.042	0.13
350.	.032	0.608	0.054	0.056	0.10
350.	.050	0.570	0.052	0.061	0.08
350.	.080	0.447	0.043	0.038	0.06
350.	.130	0.356	0.036	0.057	0.04
350.	.200	0.256	0.036	0.055	0.03
350.	.320	0.280	0.051	0.061	0.02
500.	.013	0.904	0.083	0.050	0.14
500.	.020	0.725	0.065	0.046	0.12
500.	.032	0.546	0.059	0.034	0.10
500.	.050	0.433	0.051	0.035	0.08
500.	.080	0.397	0.047	0.032	0.06
500.	.130	0.276	0.036	0.030	0.04
500.	.200	0.228	0.035	0.027	0.03
650.	.013	0.881	0.120	0.076	0.14
650.	.020	0.727	0.081	0.061	0.12
650.	.032	0.545	0.068	0.047	0.09
650.	.050	0.483	0.062	0.045	0.07
650.	.080	0.422	0.059	0.031	0.05
650.	.130	0.369	0.050	0.030	0.04
650.	.200	0.262	0.044	0.042	0.03
650.	.320	0.222	0.055	0.074	0.02
800.	.020	0.686	0.098	0.083	0.11
800.	.032	0.676	0.085	0.082	0.09
800.	.050	0.533	0.075	0.067	0.07
800.	.080	0.428	0.075	0.057	0.05
800.	.130	0.490	0.075	0.066	0.04
800.	.200	0.312	0.057	0.073	0.03
800.	.320	0.258	0.065	0.090	0.02
1200.	.032	0.668	0.109	0.091	0.09
1200.	.050	0.412	0.078	0.064	0.07
1200.	.080	0.502	0.089	0.069	0.05
1200.	.130	0.436	0.084	0.066	0.03
1200.	.200	0.260	0.057	0.048	0.02
1200.	.320	0.201	0.056	0.064	0.01
2000.	.05	0.634	0.087	0.046	0.06
2000.	.08	0.395	0.060	0.035	0.05
2000.	.13	0.237	0.048	0.026	0.03
2000.	.20	0.199	0.041	0.017	0.02
2000.	.32	0.193	0.043	0.045	0.01
5000.	.13	0.453	0.121	0.056	0.03
5000.	.20	0.229	0.087	0.030	0.02
5000.	.32	0.283	0.085	0.064	0.01

Table 8: *Proton structure function $F_2(x, Q^2)$ with statistical and systematic errors, part II. The normalization uncertainty, not included in the systematic error, is 1.5%.*